Small ARF-like 2 GTPase TITAN 5 is linked with the dynamic regulation of IRON-REGULATED TRANSPORTER 1

Inga Mohr[1], Monique Eutebach[1], Marie C. Knopf[1], Naima Schommen[1], Regina Gratz[1], Kalina Angrand[2], Lara Genders[1], Tzvetina Brumbarova[1], Petra Bauer[1,3] and Rumen Ivanov[1]

[1]Institute of Botany, Heinrich Heine University, Universitätsstr. 1, 40225 Düsseldorf, Germany.
[2]former address: Department of Biosciences-Plant Biology, Saarland University, 66123 Saarbrücken, Germany.
[3]Cluster of Excellence on Plant Sciences (CEPLAS), Heinrich-Heine University, 40225 Düsseldorf, Germany.

Author contributions: P.B. and R.I. conceived the project; I.M., T.B., P.B. and R.I. designed experiments, supervised the research and analyzed data; I.M., M.E., M.C.K., N.S., R.G., and K.A. performed experiments; L.G. contributed key materials; I.M. wrote the manuscript; I.M., P.B. and R.I. edited the manuscript; P.B. acquired funding. P.B. and R.I. agreed to serve as the author responsible for contact and communication.

Highlights

- TTN5 interacts with the large intracellular loop and variable region of IRON-REGULATED TRANSPORTER 1 (IRT1)
- TTN5 has a positive effect on root iron (Fe) reductase activity.
- TTN5 and IRT1 colocalize at the plasma membrane and in the endomembrane system related to vesicle transport
- TTN5 can interact with peripheral membrane proteins of the IRT1 interactome, EHB1, PATL2 and SNX1 suggesting a coordinating role in IRT1 regulation

Running title

ARF-like GTPase TTN5 and iron acquisition

One-sentence summary

TTN5, a small ARF-like GTPase, is connected to the dynamic regulation of IRON-REGULATED TRANSPORTER 1 (IRT1) in the vesicular trafficking system through direct protein interaction and colocalization, linking with various peripheral membrane proteins of the IRT1 interactome and iron reductase activity.

Keywords

ARF-like; ARLC1; ARL2; EHB1; endomembrane; GTPase; HALLIMASCH; iron; PATL2; plasma membrane; SEC14; SNX1; vesicle

Abstract

Iron acquisition is crucial for plants. The abundance of IRON-REGULATED TRANSPORTER 1 (IRT1) at the plasma membrane is controlled through endomembrane trafficking. Vesicular trafficking requires small ARF-like GTPases, one of them is TITAN 5

(TTN5). Its physiological functions during the life cycle and cellular targets remain unknown. Little is known how the vesicular trafficking mechanism affects IRT1 localization.
We show that TTN5 interacts with the large cytoplasmic variable region and protein-regulatory platform of IRT1. *ttn5-1*$^{+/-}$ plants have a reduced activity of root iron reductase, needed for iron uptake via IRT1. Fluorescent fusion proteins of TTN5 and IRT1 colocalize at the plasma membrane and in endosomes/multivesicular bodies, where IRT1 sorting and cycling between the plasma membrane and the vacuole are coordinated. Colocalization at the plasma membrane depends partly on the interaction ability of TTN5. TTN5 can also interact with peripheral membrane proteins that are components of the IRT1 regulation machinery, like the trafficking factor SNX1, the C2 domain protein EHB1 and the SEC14-GOLD protein PATL2. Hence, this work links iron acquisition and vesicular trafficking involving a small GTPase of the ARF family. This opens up the possibility to study the involvement of TTN5 in nutritional cell biology in the endomembrane system.

Abbreviations

AD	activation domain
Arabidopsis	*Arabidopsis thaliana*
ARF-like / ARL	ADP-ribosylation factor-like
BD	binding domain
EE	early endosomes
EHB1	ENHANCED BENDING 1
FRET-APB	Förster Resonance Energy Transfer-Acceptor Photobleaching
GAP	GTPase-activating protein
GEF	guanine nucleotide exchange factor
MVB	multivesicular body
PATL2	PATELLIN 2
ROI	region of interest
SNX1	SORTING NEXIN 1
TGN	*trans*-Golgi network
TTN5	TITAN 5
Y2H	yeast two-hybrid
ZIP	ZRT/IRT-LIKE PROTEIN

Introduction

Plants adjust to environmental changes, such as variations of soil nutrient availability. Cellular membranes are very dynamic in plants, and this is crucial for sessile organisms. Plants can scan their environment for nutrients and control the activities of plasma membrane transporter proteins by vesicular trafficking. Many open questions still exist with regard to the environmental responsiveness and the complexity of the plant cell endomembrane system.

One essential element, iron (Fe), is abundant in the soil. But since Fe is mostly present in its ferric Fe^{3+} form in soil, it tends to be immobilized into insoluble complexes. Fe^{3+} must therefore be mobilized into a bioavailable form. Plants like *Arabidopsis thaliana* (Arabidopsis) are capable of this. One mechanism consists in reducing Fe^{3+} *via* plasma membrane FERRIC REDUCTION OXIDASE 2 (FRO2) (Robinson et al. 1999). The reactive ferrous Fe^{2+} is taken up

by IRON-REGULATED TRANSPORTER 1 (IRT1) into root epidermis cells (Eide et al. 1996, Vert et al. 2002).

IRT1 is one of the founding members of an evolutionarily conserved divalent metal ion transporter family named ZIP (ZINC-REGULATED TRANSPORTER, ZRT, IRT-LIKE PROTEIN) family (Eide et al. 1996, Guerinot 2000). Divalent metal ions are potentially cytotoxic. The activity of IRT1, like that of other ZIP proteins, is controlled at the level of protein abundance at the plasma membrane (Connolly et al. 2002, Barberon et al. 2011, Shin et al. 2013, Barberon et al. 2014, Hu 2021). Importantly, IRT1 protein activity is likely controlled through transport from the *trans*-Golgi network/early endosomes (TGN/EE) to the plasma membrane, degradation by the lytic pathway or recycling back to the plasma membrane (Ivanov et al. 2014). However, the molecular machinery for this process is barely known.

The large cytosolic variable region (vr) between transmembrane domains three and four is a characteristic regulatory feature of ZIP proteins (Guerinot 2000, Gaither and Eide 2001). In IRT1, this regulatory variable region, IRT1vr, is crucial for the control of IRT1 abundance. IRT1vr has metal ion binding sites and residues that can be phosphorylated and ubiquitinated, which are processes that precede vesicular trafficking (Grossoehme et al. 2006, Kerkeb et al. 2008, Dubeaux et al. 2018, Cointry and Vert 2019). In a search for new components binding with IRT1vr we identified peripheral membrane proteins that directly or indirectly control the activity of IRT1 (Khan et al. 2019; Hornbergs et al. 2023). Among them is C2-domain protein ENHANCED BENDING 1 (EHB1) (Khan et al. 2019) which belongs to the ten-member calcium-dependent C2-DOMAIN ABSCISIC ACID-RELATED (CAR) protein family (EHB1 is also known as CAR6) (Rodriguez et al. 2014). CAR proteins act as tethers between the membrane and signaling or transport proteins that are involved in drought, defense or nutrition (Cui and Bauer 2023). They can also oligomerize and cause membrane deformations, making them candidate proteins involved in vesicle budding (Chen et al. 2023). EHB1 interacts with IRT1vr and it has an inhibitory effect on Fe acquisition (Khan et al. 2019). Another IRT1vr interactor is PATELLIN 2 (PATL2). It has a SEC14 domain coupled with a GOLD domain. The SEC14 domain forms a lipid-binding pocket that serves to present or transfer lipophilic substances at membranes (Montag et al. 2023). For example, PATL2 can bind α-tocopherol and it has been proposed that it prevents oxidative stress upon Fe acquisition, possibly by transferring and exchanging phospholipids and α-tocopherol at the membrane (Hornbergs et al. 2023). PATL2 may also initiate vesicle formation, as it binds proteins of the endomembrane system (Hornbergs et al. 2023). Another hint for the involvement of endomembrane trafficking in IRT1 protein control stems from the observation that SORTING NEXIN 1 (SNX1), a crucial component of the retromer complex for transmembrane protein sorting, binds to endomembrane structures containing IRT1, and it is a positive regulator of IRT1 recycling at the TGN (Ivanov et al. 2014). However, IRT1 does not seem to bind SNX1 directly.

Altogether, it looks like IRT1vr has a regulatory role as protein interaction platform to recruit components for vesicular trafficking of IRT1. Fe acquisition is affected by regulation of the vesicular transport mechanism, but how this is achieved and which proteins are involved are open questions that still remain largely elusive. Whether and how the various IRT1vr-interacting peripheral membrane proteins may be connected with each other to control localization of a plasma membrane protein like IRT1, is not clear yet.

Cycling of plasma membrane proteins is an important function of endomembrane trafficking (Valencia et al. 2016, Ivanov and Vert 2021). One protein family involved in this process in mammalian cells and yeast is the Ras superfamily of small GTPases. Small GTPases are

important in vesicle-related processes as they function as molecular switches due to their GTPase activities to transmit signals. Small GTPases have usually low intrinsic nucleotide exchange and hydrolysis activity, and therefore, require the support of guanine nucleotide exchange factors (GEFs) and GTPase-activating proteins (GAPs). GEFs recruit the inactive, GDP-bound, GTPase to their site of action and lead to nucleotide exchange by GDP release. GTP binding leads to a conformational change of two regions referred to as switch I and II. The active, GTP-loaded, GTPases then exert their function, e.g. the recruiting and subsequent assembly of coat proteins by ARF1 or SAR1, until hydrolysis of the GTP by GAPs. Most of the known interactions occur in the active conformation of the GTPases (Sztul et al. 2019, Nielsen 2020, Adarska et al. 2021). Although the ARF-GTPase family is well-studied in mammals, there are only few well-established examples of an ARF-GTPase functioning in plasma membrane protein trafficking in plants, like that of ARF1-GNOM-mediated recycling of auxin carrier PIN FORMED 1 (PIN1), with GNOM being an ARF-GEF (Steinmann et al. 1999, Geldner et al. 2003). The presence of 21 ARF and ARF-like (ARL) GTPases encoded by the Arabidopsis genome raises the question whether other ARF members may act in endomembrane trafficking and what are their functions in the diverse physiological and nutrient assimilation pathways besides auxin signaling and cell division.

TITAN 5 (TTN5), also known as HALLIMASCH (HAL)/ARL2/ARLC1, is an ARF-like protein. It was identified in two independent screens for abnormal-embryo mutants arrested soon after egg cell division, indicating a central cellular function (Mayer et al. 1999, McElver et al. 2000), in agreement with its ubiquitous expression in plants (Mohr et al. 2024). TTN5 is more closely related in sequence to human ADP-ribosylation factor-like 2 (HsARL2) than any Arabidopsis protein. HsARL2 is associated with very diverse roles in cells, ranging from microtubule development, also identified for yeast and *Caenorhabditis* homologs (Bhamidipati et al. 2000, Fleming et al. 2000, Radcliffe et al. 2000, Antoshechkin and Han 2002, Tzafrir et al. 2002, Mori and Toda 2013), adenine nucleotide transport in mitochondria (Sharer et al. 2002) and control of phosphodiesterase activity in cilia (Ismail et al. 2011, Fansa and Wittinghofer 2016). HsARL2 is not only involved in a diverse set of functions and signaling cascades but it also binds very different protein partners for that. The same can be expected for TTN5. *TTN5* is expressed in the root epidermis (Mohr et al. 2024), like *IRT1* (Vert et al. 2002). TTN5 is present at the plasma membrane and in the endomembrane compartment. TTN5 is among the rare plant small GTPases for which GTPase activities are known. TTN5 can be considered atypical as it does not require a GEF to be in its active GTP-bound form and has a slow GTPase activity relying on a GAP (Mohr et al. 2024). Its unusually high intrinsic GDP-GTP exchange activity, that causes TTN5 to be present predominantly in a GTP-binding form, seems a prerequisite for its dynamic cellular localization and association with the dynamic endomembrane system and potential vesicular trafficking (Mohr et al. 2024). Physiological functions of this small GTPase, on the other hand, relevant during the entire plant life cycle, remain elusive until today.

A yeast two-hybrid screen had identified EHB1/CAR6 and PATL2 as IRT1 regulators (Khan et al. 2019, Hornbergs et al. 2023). We report here, that with this same strategy, we retrieved the HsARL2-related, small GTPase TTN5. We validated protein interactions of TTN5 and IRT1vr as well as the IRT1vr interactome and found a physiological Fe reductase phenotype linked with root Fe acquisition. Colocalization analysis indicated that active GTP-bound TTN5 was more colocalizing with IRT1 in intracellular vesicles than a mutant TTN5 form. Hence, our work indicates that the dynamic small GTPase TTN5 acts in a nutritional-environmental context in the vesicular trafficking system that controls the root Fe transporter IRT1.

165 ## Results

166 **TTN5 interacts with the variable region of IRT1**

167 To identify new cytoplasmic proteins regulating IRT1 we had developed a strategy to identify
168 candidate interaction partners of IRT1vr (residues 145-192) and used IRT1vr as bait against a
169 cDNA expression library prepared from Fe-deficient Arabidopsis roots (Khan et al. 2019,
170 Hornbergs et al. 2023). We report here that 25 of the colonies (representing 25%) obtained in
171 the reported yeast two-hybrid (Y2H) screen carried a fragment of the coding sequence of the
172 gene AT2G18390, encoding the ARL-type small GTPase TTN5. The interaction was confirmed
173 in a targeted Y2H assay (Figure 1A). Small GTPases can act as molecular switches in cells
174 due to their rapid reactions and interactions with effectors, whereby TTN5 may not require a
175 GEF for nucleotide exchange as it has high affinity for GTP (illustrated in Figure 1B) (Mohr et
176 al. 2024). We further verified the protein interaction in plant cells using Bimolecular
177 Fluorescence Complementation (BiFC) as a reconstitution of YFP in positively transformed
178 cells that expressed the control marker mRFP (Figure 1C). We used previously characterized
179 mutants of conserved amino acids in the GTP-binding pocket, Thr30-to-Asn (T30N, previously
180 found to be dominant-negative or fast cycling) and Gln70-to-Leu (Q70L, with reduced GTP
181 hydrolysis activity) (Figure 1B) (Mohr et al. 2024). Both, the cYFP-TTN5^{T30N} and cYFP-TTN5^{Q70L}
182 forms interacted with nYFP-IRT1vr (Figure 1D-E). The BiFC interactions were specific as
183 neither protein partner was able to bind negative controls in this assay (Figure 1F-G). We
184 further elucidated whether IRT1vr might discriminate between the conserved TTN5 variant
185 forms using a quantitative analysis of the interaction by Förster Resonance Energy Transfer-
186 Acceptor Photobleaching (FRET-APB). This approach is based on close-proximity-dependent
187 energy transfer of an excited GFP-tagged TTN5 donor to a mCherry acceptor, here IRT1vr-
188 mCherry. Energy transfer was quantified as FRET efficiency (Figure 1H-J). FRET efficiencies
189 between all GFP-TTN5 forms and IRT1vr-mCherry were significantly higher compared to the
190 donor-only sample, confirming protein interactions between all TTN5 forms and IRT1vr. As a
191 final evidence, we performed an *in planta* pulldown experiment to show interaction of full-length
192 IRT1 and TTN5 (Figure 1K) using an Arabidopsis plant line expressing IRT1-mCherry together
193 with hemagglutine-tagged (HA)-TTN5. The mCherry part was integrated in the first small
194 cytosolic loop of IRT1 at position 80 (proIRT1::IRT1Q80-mCherry, briefly IRT1-mCherry), and
195 this fusion protein was functional as it fully complemented the severe *irt1-1* (SALK_054554) Fe
196 deficiency phenotype (Fukao et al. 2011) (Supplemental Figure S1). HA_3-TTN5 (pro35S::HA_3-
197 TTN5, briefly HA_3-TTN5) was functional as it complemented the *ttn5-1* phenotype as previously
198 described (Mohr et al. 2024). We pulled down protein complexes from whole seedlings using
199 anti-HA beads. This resulted in an increased protein abundance of HA_3-TTN5 (28 kDa) in the
200 elution fraction, as expected (Figure 1K). Importantly, IRT1-mCherry was simultaneously
201 coprecipitated and detected in this elution fraction while it was not detected in a control
202 pulldown experiment without HA_3-TTN5 (Figure 1K), indicating that the two full-length proteins
203 interact closely in Arabidopsis plant cells.

204 In sum, we can conclude that TTN5 is an interactor of IRT1 with IRT1vr as interaction
205 surface. We hypothesize that TTN5 is a potential link in the coordination of IRT1 regulation with
206 vesicle trafficking typical for ARF GTPases.

207

208 **TTN5 affects Fe homeostasis**

209 Following up on the IRT1-TTN5 interaction, we tested whether TTN5 might affect plant
210 growth under Fe-deficient conditions and/or the regulation of the Fe deficiency response.
211 Homozygous *ttn5* knock-outs are embryo-lethal (Mayer et al. 1999, McElver et al. 2000), and
212 initial growth experiments with heterozygous plants (*ttn5-1*$^{+/-}$) showed no obvious
213 developmental defects in comparison with wild type sibling plants under regular growth
214 conditions (Figure 2A, Supplemental Figure S2; (Mohr et al. 2024)). Likewise, when plants were
215 germinated in Fe-sufficient and -deficient conditions, we did not note any difference in root
216 length. Both, wild type and *ttn5-1*$^{+/-}$ siblings, had increased root length under Fe-deficient
217 conditions (Figure 2B), as expected in our growth system (Gratz et al. 2019), but there was no
218 difference between them. SPAD values indicating chlorophyll contents were also similar in the
219 wild type and *ttn5-1*$^{+/-}$ seedlings, indicating that the *ttn5* mutation has no effect on leaf color
220 (Figure 2C). Also at advanced growth stages, *ttn5-1*$^{+/-}$ plants did not differ in growth and leaf
221 color from their wild type siblings, neither in in control soil (pH 6.2) nor in an alkaline, calcareous
222 soil (ACS, pH 8). The latter conditions require Fe mobilization capacities since Fe acquisition
223 is inhibited at high pH values in the presence of bicarbonates, resulting in smaller plants with
224 leaf chlorosis ((Ohwaki and Sugahara 1997, Schmid et al. 2014), Supplemental Figure S2B).
225 Both wild type and *ttn5-1*$^{+/-}$ plants showed similarly lower aerial biomass increase and lower
226 chlorophyll on ACS conditions over a period of 43 days compared to the control conditions
227 (Supplemental Figure S2A-D). We examined the heterozygous seedlings at the molecular and
228 physiological level. *TTN5* expression was nearly 50% reduced in *ttn5-1*$^{+/-}$ compared to wild type
229 siblings, consistent with single allele presence (Figure 2D). Very interestingly, we detected a
230 15% decrease of *TTN5* gene expression under Fe deficiency compared with Fe sufficiency in
231 both, wild type and *ttn5-1*$^{+/-}$, indicating that TTN5 might be perhaps less needed under low Fe
232 supply (Figure 2D). *FRO2* encodes an Fe uptake component, the ferric reductase oxidase
233 enzyme (Robinson et al. 1999), that closely interacts with IRT1 in the root plasma membrane
234 (Martín-Barranco et al. 2020). *FRO2* and *IRT1* gene expression increase in response to Fe
235 deficiency, and this serves as a molecular marker for the root Fe deficiency status, e.g. (Gratz
236 et al. 2019). No difference of gene expression levels of *FRO2* and *IRT1* occurred in *ttn5-1*$^{+/-}$
237 roots compared with wild type, and both genes were induced under low Fe versus high Fe as
238 expected (Figure 2E-F). This indicated that root Fe deficiency responses might not be
239 compromised in *ttn5-1*$^{+/-}$. However, we then noted that in two out of three experiments (each
240 including the indicated biological replicates), root Fe reductase activity was altered. It was up-
241 regulated under Fe-deficient versus -sufficient conditions in wild type and *ttn5-1*$^{+/-}$ roots, as
242 expected, e.g. (Robinson et al. 1999, Gratz et al. 2019) but the induction was lower in *ttn5-1*$^{+/-}$
243 compared with wild type siblings (Figure 2G).
244 Taken together, heterozygous *ttn5-1*$^{+/-}$ seedlings have an Fe reductase phenotype that
245 indicates a positive effect of TTN5 at the physiological level on Fe acquisition responses in the
246 plasma membrane. This was interesting, because the two other interactors of IRT1vr,
247 EHB1/CAR6 and PATL2, had an opposite effect on Fe reductase activity (Khan et al. 2019,
248 Hornbergs et al. 2023).
249

250 **TTN5 colocalizes with IRT1 in the plasma membrane and in vesicles**

251 To investigate whether TTN5 may be located in similar places as IRT1 in root cells, as
252 expected for interacting proteins, we grew and compared side by side localization of fluorescent
253 signals in Arabidopsis plant roots expressing either IRT1-mCitrine (proIRT1::IRT1-mCitrine/*irt1-*
254 *1*), described in (Dubeaux et al. 2018), or YFP-TTN5 (pro35S::YFP-TTN5), described in (Mohr

255 et al. 2024). A similar approach has been used to compare intracellular localization of IRT1 and
256 PATL2 fusion proteins in root cells (Hornbergs et al. 2023). As previously described, fluorescent
257 signal of IRT1-mCitrine was present at the plasma membrane of root epidermis cells in our
258 growth system (Supplemental Figure S3A) (Dubeaux et al. 2018, Hornbergs et al. 2023).
259 Fluorescent plasma membrane signal was also detected for YFP-TTN5 expressing seedlings
260 (Supplemental Figure S3B), as corresponding to the previously identified pattern (Mohr et al.
261 2024). Virtual cross sections of both roots highlighted the described polar localization for IRT1-
262 mCitrine, visible in only a very few epidermis cells, as previously seen (Supplemental Figure
263 S3C; (Dubeaux et al. 2018, Hornbergs et al. 2023) compared with an equally distributed YFP
264 localization in the plasma membrane of YFP-TTN5 expressing seedlings in the epidermis
265 (Supplemental Figure S3D). Next to plasma membrane localization both, fluorescent signals of
266 IRT1-mCitrine and YFP-TTN5 expressing seedlings, were also present in vesicle-like
267 structures in root cells (Supplemental Figure S3E-F). These findings suggest that indeed, IRT1
268 and TTN5 may locate to similar structures inside root cells, supporting an interaction at these
269 places.
270 To confirm the obtained Arabidopsis data and to investigate potential colocalization of TTN5
271 with IRT1 in the same cells, we used the transient expression system of *Nicotiana benthamiana*
272 (*N. benthamiana*). This system has the advantage that fusion proteins of TTN5 and IRT1 are
273 well detectable, and through well-established pharmacological approaches the localization
274 patterns of TTN5 and IRT1 proteins can be confirmed (Ivanov et al. 2014, Mohr et al. 2024).
275 We used a GFP-tagged IRT1 with GFP inserted inside IRT1vr (hereafter termed IRT1-GFP).
276 This IRT1 fusion protein was present at the plasma membrane. Fluorescent spots were also
277 found in close proximity to the plasma membrane (Supplemental Figure S4A), consistent with
278 previous reports (Barberon et al. 2011, Ivanov et al. 2014). To further evaluate its usefulness
279 for localization studies, we compared IRT1-GFP signals with already described C-terminally-
280 tagged IRT1-mCherry signals in *N. benthamiana* pavement cells before and after wortmannin
281 treatment, see (Ivanov et al. 2014). Wortmannin is a fungal metabolite with an inhibitory effect
282 on phosphatidylinositol-3-kinase (PI3K) function, leading to swollen multivesicular bodies
283 (MVBs) and therefore is commonly used to investigate endocytosis (Cui et al. 2016). Signals
284 upon expression of these two fusion proteins showed colocalization (Supplemental Figure S4B)
285 and, following wortmannin treatment, were observed among others in swollen structures,
286 suggesting partial presence in the MVBs (Supplemental Figure S4C), indicating that the IRT1-
287 GFP fusion protein was viable for IRT1 localization studies. IRT1-GFP also partially
288 complemented an early rosette growth deficit of *irt1-1* (in pro35S::IRT1-GFP/*irt1-1* plants),
289 indicating partial functionality of the IRT1-GFP construct for this trait (Supplemental Figure
290 S4D).
291 We detected colocalization of IRT1-GFP and mCherry-TTN5 including TTN5-mutant
292 fluorescent signals at the plasma membrane or just below (Figure 3A-C). Previously, we had
293 described YFP-TTN5 localization in vesicle-like structures and close proximity of YFP-TTN5 to
294 the plasma membrane (Mohr et al. 2024). Moving fluorescent structures upon YFP-TTN5^{T30N}
295 expression were less mobile than for YFP-TTN5 and YFP-TTN5^{Q70L} (Mohr et al. 2024). Very
296 interestingly, the different mCherry-TTN5 forms have different abilities to colocalize with IRT1
297 by Pearson coefficients (Figure 3D). While Pearson coefficients of signals of IRT1-GFP with
298 mCherry-TTN5 and mCherry-TTN5^{Q70L} were 0.80 and 0.77, it was higher, namely 0.90, for
299 IRT1-GFP and mCherry-TTN5^{T30N}, demonstrating higher general colocalization between IRT1-
300 GFP and the low-mobile TTN5^{T30N} form (similar results for overlap coefficients Supplemental

301 Figure S4E). Signals of all three mCherry-TTN5 forms were also localized in IRT1-GFP-positive
302 structures close to the plasma membrane, suggesting colocalization in plasma membrane-
303 derived vesicles (Figure 3E-G). Surprisingly, the Pearson coefficients changed when these
304 spotted structures were analyzed (Figure 3H; Supplemental Figure S4F similar results for
305 overlap coefficients). While the values for fluorescent signals of mCherry-TTN5 (0.80) and
306 mCherry-TTN5^{Q70L} (0.78) constructs with IRT1-GFP remained relatively the same, we obtained
307 with 0.78 now a similar coefficient with mCherry-TTN5^{T30N}. Similar results were achieved while
308 checking the overlaps of mCherry-TTN5 structures with IRT1-GFP and vice versa with a
309 centroid-based analysis. We obtained overlaps of 36-41% for mCherry-TTN5 signals with IRT1-
310 GFP (Supplemental Figure S4G). 54% of IRT1-GFP-positive structures colocalized with signals
311 of mCherry-TTN5^{T30N}, whereas 64% and up to 83% colocalized with mCherry-TTN5 and
312 mCherry-TTN5^{Q70L}, respectively. From this, we hypothesized that IRT1 is more likely to be
313 colocalized with TTN5^{T30N} at the plasma membrane than with TTN5 wild type or TTN5^{Q70L}. as
314 the latter may be active in promoting intracellular cycling. This was consistent with the previous
315 observation that signals of mCherry-TTN5^{T30N} were moving slower in certain cells than those
316 of the other two TTN5 fusion proteins. We therefore deduce that TTN5^{T30N} may slow down the
317 removal of IRT1 from the plasma membrane. In an attempt to identify the intracellular structures
318 in which colocalization of TTN5 and IRT1 occurred, we treated the cells with wortmannin
319 (Figure 3I). Structures positive for both IRT1-GFP and mCherry-TTN5 fluorescent signals
320 became doughnut-shaped suggesting IRT1-TTN5 colocalization in MVBs (Figure 3J-K).
321 Presence of IRT1 in these late endosomal compartments has been observed previously, and
322 might be part of the pathway to IRT1 vacuolar degradation (Dubeaux et al. 2018), same for
323 mCherry-TTN5 (Mohr et al. 2024). Thus, our findings emphasize the involvement of TTN5 in
324 the endomembrane trafficking of the Fe transporter IRT1.
325

326 **TTN5 interacts with IRT1 regulators EHB1, SNX1 and PATL2**

327 IRT1 can associate and colocalize with peripheral membrane proteins SNX1, EHB1 and
328 PATL2 that can be associated with events of vesicular trafficking (Ivanov et al. 2014, Khan et
329 al. 2019, Hornbergs et al. 2023). This opened up the possibility that TTN5 may associate not
330 only with IRT1 but also with proteins of IRT1 interactome in close proximity in cells, prompting
331 us to investigate this further.

332 At first, we tested IRT1-interacting EHB1. CAR proteins like EHB1 have a plant-specific
333 insertion of an extra region within the C2 domain known as signature (sig) domain, that is
334 involved in binding proteins including IRT1 (Rodriguez et al. 2014, Khan et al. 2019). We
335 demonstrated above that nYFP-EHB1Δsig did not interact with cYFP-TTN5 in BiFC (Figure 1F).
336 However, when using for interaction with cYFP-TTN5 the intact nYFP-EHB1 protein or the
337 EHB1 sig-nYFP domain alone we did find evidence of protein interaction in close proximity to
338 the plasma membrane using BiFC in contrast to EHB1Δsig (Figure 4A-C). Surprisingly, the
339 cYFP-TTN5 mutant forms both failed to complement with nYFP-EHB1 in the split-YFP assay
340 (Figure 4D-E). This was surprising because FRET-APB experiments validated the interaction
341 between EHB1-GFP as the donor and TTN5-mCherry as well as of the two TTN5 mutant
342 variants as the acceptors (Figure 4F). Surprisingly, the FRET pairs EHB1-GFP with TTN5^{T30N}-
343 mCherry and TTN5^{Q70L}-mCherry resulted in an even higher FRET-efficiency compared to
344 TTN5-mCherry (Figure 4F). Perhaps, the mutant behavior and difference between BiFC and
345 FRET-APB were due to the different tag orientations in these two types of assays.

346 In another BiFC experiment, cYFP-TTN5 was able to complement split-YFP together with
347 SNX1-nYFP close to the plasma membrane (Figure 4G). The cYFP-TTN5^{T30N} mutant failed in
348 BiFC (Figure 4H), while the hydrolysis impaired TTN5 GTPase variant interacted with SNX1-
349 nYFP (Figure 4I). SNX proteins are classified by their characteristic domains. SNX1 represents
350 the class I SNX proteins, characterized by the presence of PHOX-homology (PX) and Bin-
351 Amphiphysin-Rvs (BAR) domains (Heucken and Ivanov 2018). Such a domain organization is
352 typical for proteins that function in membrane and phosphoinositide binding by the PX domain,
353 whereas the BAR domain is involved in membrane curvature sensing and the formation of
354 endosomal tubules (Peter et al. 2004, Frost et al. 2009). Interestingly, ARF-GAPs which are
355 needed for the GTP hydrolysis, contain a BAR domain as well (Memon 2004). We found
356 evidence that cYFP-TTN5 binds to both the SNX1 PX-nYFP and BAR-nYFP domains using
357 BiFC (Figure 4J-K).
358 Lastly, plasma membrane-localized SEC14 protein PATL2 binds IRT1vr (Hornbergs et al.
359 2023). We tested interaction ability of cYFP-TTN5 with PATL2-nYFP in BiFC experiments. YFP
360 signals indicating complementation and interaction were visible at the plasma membrane, fitting
361 to the localization studies of both PATL2 and TTN5 (Figure 4L). We were not able to observe
362 YFP signal complementation for the combination of PATL2-nYFP and any of the two GTPase
363 variants cYFP-TTN5^{T30N} (Figure 4M) and cYFP-TTN5^{Q70L} (Figure 4N). This was very interesting
364 as it is either a limitation of the method or could indicate that the TTN5 switching mechanism
365 may be required for a potential interaction between the proteins. However, this needs to be
366 tested further in the future. To further identify the region of interaction, we tested already
367 published deletion mutants of PATL2 (Montag et al. 2020). PATL2 can be divided into two
368 protein halves, consisting of either an N-terminal part with no particular conformation or the C-
369 terminal part with CRAL-TRIO-N-terminal extension (CTN)-SEC14-Golgi dynamics (GOLD)
370 domains that is conserved between SEC14-GOLD proteins in plants (Montag et al. 2020). The
371 N-terminal part is needed for the interaction with IRT1vr (Montag et al. 2020). We used the
372 PATL2 deletion mutants PATL2ΔC lacking the CTN-SEC14-GOLD part and PATL2ΔN lacking
373 the IRT1vr-interacting N-terminal part. PATL2ΔC-nYFP together with cYFP-TTN5
374 complemented YFP fluorescence indicating interaction (Figure 4O), whereas no signal was
375 obtained by PATL2ΔN-nYFP in combination with cYFP-TTN5 (Figure 4P), similar as in the case
376 of IRT1vr (Hornbergs et al. 2023). Interestingly, the fluorescent complementation signal
377 between cYFP-TTN5 and PATL2ΔC-nYFP was no longer present at the plasma membrane
378 consistent with the observation that the PATL2 plasma membrane localization is dependent on
379 C-terminal PATL2 domain region (Montag et al. 2020).
380 We also analyzed *EHB1, SNX1* and *PATL2* gene expression. All genes were expressed in
381 similar levels in both wild type and *ttn5-1*$^{+/-}$ (Supplemental Figure S5A-C) indicating that there
382 was no feedback at the level of regulation of genes encoding the TTN5 interactors.
383 In summary, we could show that TTN5 is not only able to interact with IRT1vr but also with
384 three peripheral membrane proteins that can be present in the vicinity of IRT1 at membrane
385 sites in root cells.
386

387 **Discussion**

388 Here, we report that the small GTPase TTN5 is a potential link in IRT1-related Fe
389 homeostasis and trafficking of the transporter within the endomembrane system (Figure 5).
390 Such a finding is highly interesting. It was known that IRT1 is post-translationally controlled

involving the vesicular trafficking system, but components that may bind with IRT1 during this process had remained obscure. Moreover, the connections of small GTPases like TTN5 with endomembrane trafficking were mostly not ascribed to concrete physiological roles. Hence, our report is very timely, and highlighting direct protein connections between cargo and vesicle trafficking components fills a gap in our understanding.

TTN5, that is part of the endomembrane system, targets IRT1vr

The protein interaction between TTN5 and IRT1 is supported by multiple findings. First, the interaction was detected in a Y2H screen, that yielded only few interaction partners, which could all be validated (Khan et al. 2019, Hornbergs et al. 2023). Second, the interaction was verified by using independent methods (targeted Y2H, BiFC, FRET-APB and Co-IP). Third, fluorescent signals of mCherry-TTN5 and IRT1-GFP reporter proteins colocalized in cells, and their localization overlapped in intracellular membrane-associated locations in cells of the root epidermis, in which both genes are expressed. Further, TTN5 was found to interact with proteins of the IRT1vr environment (Figure 5A-B). These findings altogether indicate that in plant roots, TTN5 and IRT1 indeed may interact in root epidermis cells in places related with Fe acquisition. The previously described TTN5 localization pattern in vesicles and at the plasma membrane (Mohr et al. 2024) was confirmed upon colocalization with IRT1 in this study. Hence, IRT1 localization dependent on endomembrane trafficking might be linked with the presence of TTN5 in this process.

A very interesting finding was that the mCherry-TTN5^{T30N} variant tended to colocalize more at the plasma membrane with IRT1-GFP. This could explain previous colocalization data with a MVB marker overlapping more with YFP-TTN5 and the hydrolysis impaired mutant YFP-TTN5^{Q70L} (Mohr et al. 2024) and reinforces our suggestion that TTN5 has functions in vesicle trafficking. Although a GEF is not needed for nucleotide exchange of TTN5 (Mohr et al. 2024), TTN5^{T30N} may have a conformation that facilitates binding of a GEF so that TTN5^{T30N} along with IRT1 might be retained at the plasma membrane by the unknown TTN5-interacting GEF. The presence of mCherry-TTN5 signals together with IRT1-GFP in wortmannin-induced swollen structures, probably indicating MVBs, is supporting the idea of a role in transporter degradation. MVBs are known to be the last step before vacuolar degradation (Kolb et al. 2015, Arora and Van Damme 2021). This could indicate that TTN5 presence is a critical point of IRT1 sorting fate. We therefore propose a role of TTN5 in targeting intracellular IRT1 protein (Figure 5B). In such a process, TTN5 could be present at the plasma membrane in a resting state. In the move of GTPase activation, it could be recruited to the place of action and active TTN5 would play a role in IRT1 cycling. TTN5 should predominantly bind GTP and be in an active state in the cell (Mohr et al. 2024). Further, there is support of a role of TTN5 in IRT1 recycling by the binding of TTN5 and SNX1. SNX1 is involved in the recycling of IRT1 at these sites (Ivanov et al. 2014). Hence, TTN5 can be in a functional complex with SNX1 to control the recycling of the cargo protein IRT1.

The observed roles of TTN5 fit well with the general understanding of ARF-signaling in plasma membrane protein trafficking. The auxin transporters PIN1 and PIN2 and the boron transporter BOR1, like IRT1, are polarly localized in the plasma membrane and undergo a constant degradation-recycling process (Benková et al. 2003, Takano et al. 2010, Barberon et al. 2014). Apart from vesicle formation, as described for ARF1 or SAR1, a role in this process was shown for other regulatory mechanisms of ARF-signaling through the GEFs and GAPs (Nielsen 2020). GNOM and BIG5, two ARF-GEFs, and ARF1-regulators, are described to be

437 involved in the proper localization of the plasma membrane transporter PIN1, functioning at
438 different regulatory steps (Geldner et al. 2003, Anders et al. 2008, Kleine-Vehn et al. 2008,
439 Tanaka et al. 2009). In addition, another ARF GTPase ARF1A1C may not only partially
440 colocalize with GNOM, but modified activity also resulted in impaired localization of PIN1 to the
441 plasma membrane and also altered vacuolar targeting of PIN2 (Tanaka et al. 2014). BOR1
442 plasma membrane localization depends on GNOM as well (Yoshinari et al. 2021), showing a
443 good connection between ARF-GEFs and plasma membrane protein localization.
444 Taken together, TTN5 that is part of the endomembrane system (Mohr et al. 2024) is linked
445 with a transporter protein whose abundance is controlled by endomembrane trafficking. For
446 future studies, stable coexpression of both proteins under the control of the endogenous
447 promoter will be suitable to investigate the effect of TTN5 on IRT1 localization. Finally, due to
448 the very low intrinsic GTP hydrolysis activity of TTN5, identification of TTN5-GAPs will shed
449 light on TTN5 function in Fe homeostasis and potential other cellular signaling events. It will
450 also be interesting to explore whether a membrane-localized GEF exists that can act upon
451 TTN5. Future identification of potential TTN5-GEF and -GAP proteins will be of great interest
452 to clarify the role of TTN5 in endomembrane trafficking with particular reference to cues
453 controlling IRT1.
454

455 **TTN5 might play a general role in Fe nutrition**

456 TTN5 does not only have an influence on IRT1 but also on other aspects in Fe nutrition. A
457 partial lack of TTN5 results in decreased Fe reductase activity. The decrease in Fe reductase
458 activity is likely caused by an effect on FRO2. It was found that IRT1 can interact with FRO2 to
459 form a complex for a highly effective Fe uptake machinery (Martín-Barranco et al. 2020).
460 Reduced Fe reductase activity could be due to an indirect influence of TTN5 on the complex
461 formation or it could be directly driven by TTN5. Interestingly, both *ehb1* and *patl2* seedlings
462 have a higher Fe reductase activity under Fe deficiency compared to wild type (Khan et al.
463 2019, Hornbergs et al. 2023). In case EHB1 and PATL2 also act on FRO2, this points to an
464 opposing role of TTN5 on the Fe deficiency response in the protein complex. Gene expression
465 analysis revealed no great impact on Fe-related genes in *ttn5-1*$^{+/-}$ roots, implying an effect of
466 TTN5 mostly on posttranslational level.
467 It is a possibility that TTN5 has very different effects depending on its localization in the cell.
468 For example, the effect on Fe reduction could be different from its effect on colocalization with
469 IRT1 in MVBs. Different types of interaction partners were reported for the human ARL2 with
470 connection to distinct cellular functions in tubulin folding and microtubule dynamics
471 (Bhamidipati et al. 2000) or in mitochondria (Sharer et al. 2002). Based on these distinct
472 locations and the associated functions of ARL2, it was proposed that ARL2 may act at a high
473 level in signaling (Francis et al. 2016). This can be also the case in Arabidopsis. For example,
474 TTN5 may bridge TTN5 microtubule function (Mayer et al. 1999) with IRT1 regulation.

475

476 **TTN5 interacts with EHB1, SNX1 and PATL2 and may coordinate IRT1 regulation**

477 The close interaction of TTN5 with EHB1 was suggested by BiFC and FRET-APB and with
478 PATL2 and SNX1 by BiFC. The interactions are further supported by deletion mutant
479 approaches. Moreover, the interacting sites of PATL2 and EHB1 with TTN5 are similar to those
480 for IRT1vr, supporting again the possibility that these domains and motifs are at the basis of a
481 protein complex forming at the IRT1vr regulatory platform.

482 Interaction with the IRT1 regulators EHB1, PATL2 and SNX1 suggests that TTN5 could not
483 only be linked with Fe nutrition but also the associated Ca^{2+}- and ROS-signaling events (Khan
484 et al. 2019, Hornbergs et al. 2023). EHB1 is additionally interesting as a member of the CAR
485 family. Several CAR proteins can initiate Ca^{2+}-dependent membrane curvature, which may
486 provide a direct link to vesicle trafficking. Interestingly, Ca^{2+} is bound by EHB1 *via* its C2 domain,
487 which is also a common feature of class III ARF-GAPs (Vernoud et al. 2003, Knauer et al.
488 2011). Indeed, EHB1 is directly linked to ARF signaling in an antagonistic interaction with ARF-
489 GAP AGD12 in gravitropic bending (Dümmer et al. 2016, Rath et al. 2020). Further research
490 needs to investigate whether TTN5 can interact with the C2-domain containing ARF-GAPs
491 AGD11-AGD13 as well. Additionally, crystallization experiments revealed a potential Ca^{2+}-
492 binding site between HsARF6 and its GAP ASAP3. The GTP hydrolysis was stimulated in the
493 presence of Ca^{2+} proposing a linkage between Ca^{2+}- and ARF-signaling (Ismail et al. 2010). We
494 therefore consider the possibility of an interaction between TTN5 and EHB1 in a Ca^{2+}-
495 dependent manner. PATL2 may interact with IRT1 to prevent lipid peroxidation stress
496 (Hornbergs et al. 2023). Prolonged Fe deficiency leads to an increase in hydrogen peroxide
497 concentration as well as an activity increase of catalase CAT2 (Le et al. 2015, von der Mark et
498 al. 2020, Gratz et al. 2021). Some catalases are present in the PATL2 interactome in roots
499 (Hornbergs et al. 2023). Future studies may address whether TTN5 is connected with oxidative
500 stress and Ca^{2+} signaling.
501 SNX1 is a positive regulator for IRT1 recycling to the plasma membrane in the sorting
502 endosomes (Ivanov et al. 2014) and for endosomal recycling of the auxin efflux carrier PIN2
503 (Jaillais et al. 2006). SNX1 is therefore part of the recycling of specific plasma membrane
504 proteins. Interestingly, deficiency of BLOS1 leads to accumulation of PIN1 and PIN2 at the
505 plasma membrane (Cui et al. 2010). BLOS1 seems to be an ortholog of the mammalian
506 biogenesis of lysosome-related organelles complex 1 (BLOC-1), which is responsible for
507 vesicle transport from endosomes to lysosomes (Li et al. 2007, Raposo et al. 2007). SNX1 can
508 interact with both BLOS1 and BLOS2 and could therefore also play a role in vesicle-mediated
509 transport through these interactions (Cui et al. 2010, Heucken and Ivanov 2018). SNX1
510 possesses a BAR domain which is also typical for class I ARF-GAPs (Vernoud et al. 2003,
511 Heucken and Ivanov 2018). A connection between the SNX1 BAR domain and an ARF6-GEF
512 was identified in mouse by their interaction. This interaction was associated with a positive
513 effect of ARF6 function (Fukaya et al. 2014). Colocalization analysis revealed overlapping
514 expression in endosomes, which fits known SNX1 localization in Arabidopsis (Fukaya et al.
515 2014, Ivanov et al. 2014), this could be a possible interconnection between ARF-signaling and
516 SNX1. Here, we identified an interaction between TTN5 and SNX1, which could be the critical
517 link in the decision between SNX1-dependent recycling and degradation of IRT1. SNX1 could
518 be needed for a potential TTN5-GEF and subsequent TTN5 recruiting to membranes. Based
519 on the opposing roles of EHB1 and SNX1 in IRT1 regulation and their connection to TTN5, we
520 suggest a coordinating role of TTN5 in transporting IRT1 between plasma membrane and
521 endosomes by interacting with peripheral membrane proteins such as EHB1, PATL2 and
522 SNX1. The findings that some ARF-GAPs have a C2 or BAR domain, and that SNX1 interacts
523 with an ARF-GEF strengthen the interest in the identification of TTN5-GEFs and -GAPs.
524 Further research has to focus on physiological aspects in either combined knockout mutants
525 or tagged-protein lines to arrange and decipher the IRT1 regulatory network. An intriguing open
526 question is whether a large IRT1vr-EHB1-PATL2-TTN5-SNX1 complex is assembled. If so, the
527 next question is how, when and in which order the individual or all components of the IRT1vr

528 complex are assembled. Another question is what the structural requirements for proper protein
529 conformations and membrane interfaces are (Figure 5A, B).

530 **Conclusion and perspectives**

531 This study provides hints that the ARF-like GTPase TTN5 contributes to endocytosis and
532 vesicle trafficking of IRT1 by way of a protein complex at IRTvr comprising TTN5 and other
533 IRT1 interactors. Evidence that small GTPases can bind with plasma membrane and peripheral
534 membrane proteins is instrumental to understand how membrane proteins are controlled by
535 vesicular trafficking components in plants. An intriguing question is whether TTN5 also targets
536 other transmembrane cargo proteins. Future work may uncover additional functions of TTN5
537 or of other GTPase protein complexes of this kind and determine the requirements and order
538 of events for complex assembly leading to vesicular trafficking.

539 Material & Methods

540 **Yeast two-hybrid (Y2H)**

541 The yeast two-hybrid screen for identification of IRT1vr interactors was performed previously
542 and is described in Khan et al. (2019). Targeted Y2H interactions were tested using the GAL4
543 transcription factor system with histidine as selection marker. *TTN5* coding sequence was
544 amplified using TITAN5 nter B1 and TITAN5 stop B2 primers (for primer sequences, see
545 Supplemental Table S1). Obtained fragment was cloned into pDONR207 *via* Gateway BP
546 reaction (Life Technologies) with following LR reactions into pGBKT7-GW (binding domain,
547 BD) or pACT2-GW (activation domain, AD). Both vectors were a kind gift from Dr. Yves Jacob.
548 The yeast strain AH109 was cotransformed with the corresponding AD- and BD-tagged
549 expression vectors. The combination pACT2:SNX1 and pGBKT7:SNX1 (Pourcher et al. 2010)
550 was used as a positive control. Negative controls were cotransformations with the respective
551 non-recombined pACT2-GW or pGBKT7-GW. Drop test was performed with SD -Leu, -Trp-
552 cultures at an OD_{600} of 0.1 and three additional 1:10 dilution steps (10^1-10^4) on SD -Leu, -Trp-
553 and SD -Leu, -Trp, -His +0,5 mM 3-amino-1,2,4-triazole-plates. One of each plate was
554 incubated either at 30°C or at room temperature, wrapped in aluminum foil for up to two weeks.

555 ***Nicotiana benthamiana* leaf infiltration**

556 *Nicotiana benthamiana* plants were grown on soil for 2-4 weeks in a greenhouse facility
557 under long day conditions (16 hours light, 8 hours darkness, 20°C). *N. benthamiana* leaf
558 infiltration was performed with the Agrobacterium (*Rhizobium radiobacter*) strain C58 (GV3101)
559 carrying the respective constructs for confocal microscopy. Agrobacteria cultures were grown
560 overnight at 28°C, centrifuged for 5 min at 4°C at 5000*g*, resuspended in infiltration solution
561 (5% sucrose, a pinch of glucose, 0.01% Silwet Gold, 150 µM acetosyringone) and incubated
562 for 1 hour at room temperature. Bacterial suspension was set to an OD_{600}=0.4 and infiltrated
563 into the abaxial side of *N. benthamiana* leaves.

564 Expression of pABind and pMDC7 (Curtis and Grossniklaus 2003, Bleckmann et al. 2010)
565 constructs was induced with a β-estradiol solution (20 µM β-estradiol, 0.1% Tween 20)
566 16 hours before imaging.

567 **Bimolecular Fluorescence Complementation (BiFC)**

568 BiFC was used to study protein interaction of TTN5 and the respective GTPase $TTN5^{T30N}$
569 and $TTN5^{Q70L}$ variants with other proteins in plant cells. At first, entry clones were generated.
570 *TTN5*, $TTN5^{T30N}$ and $TTN5^{Q70L}$ coding sequences with stop codon were amplified using the

571 primers TITAN5 n-ter B1 and TITAN5 stop B4 (Supplemental Table S1). *IRT1vr* coding
572 sequence with stop codon was amplified using the primers I1L1B3 and I1LB2. Amplifying full-
573 length *EHB1* the primer pair EHB1 n-ter B3 and EHB1 stop B2 was used. Amplification of
574 *EHB1Δsig* is described in Khan et al. 2019. *SNX1* coding sequence without stop codon for C-
575 terminal fusion was amplified using the primer SNX1 B3 and SNX1 ns B2. Cloning of SNX1
576 deletion mutants SNX1PX and SNX1BAR was done using the primers SNX1 B3 and PXSNX1
577 rev and BARSNX1 fwd and SNX1 ns B2 respectively. The used PATL2 constructs are
578 described in Hornbergs et al. (2023). The amplified PCR products were cloned *via* Gateway
579 BP reaction (Life Technologies) into pDONR221-P1P4 (Invitrogen) or pDONR221-P3P2
580 (Invitrogen).
581 The obtained constructs were then used to prepare final recombinant destination vectors in
582 an LR reaction (Life Technologies) for cloning into pBiFCt-2in1 vectors (Grefen and Blatt 2012).
583 Agrobacteria were transformed with correct constructs and used for *N. benthamiana* leaf
584 infiltration. After 48 hours, the mRFP expression control signal and YFP signals were detected
585 by fluorescent microscopy (LSM 780, Zeiss) with a 40x C-Apochromat water immersion
586 objective. YFP constructs were detected at 491-560 nm after exciting at 488 nm and mCherry
587 fluorescence was excited at 561 nm and emission detected at 570-633 nm.
588 The BiFC constructs were tested in three independent replicates with three infiltrated leaves
589 each. The vectors pBiFC-2in1-NN and pBiFC-2in1-CN were kindly provided by Dr. Christopher
590 Grefen, Tübingen, Germany.

591 **Förster-Resonance-Energy Transfer Acceptor Photo Bleaching (FRET-APB)**

592 FRET-APB was used to verify protein-protein interactions of TTN5 $TTN5^{T30N}$, and $TTN5^{Q70L}$.
593 The coding sequences without stop codon were amplified with the primers TITAN5 B1 and
594 TITAN5 ns B2, and cloned into the pDONR207 (Invitrogen, BP reaction, Life Technologies).
595 Cloning of pDONR207:IRT1vr and pDONR207:EHB1 is described in Khan et al. (2019). The
596 obtained constructs were used for LR reactions (Life Technologies) with the pABind-GFP,
597 pABind-mCherry and pABind-FRET for C-terminal tagging (Bleckmann et al. 2010). N-terminal
598 GFP-TTN5 constructs were cloned by overlap extension PCR simultaneously with mCherry-
599 TTN5 constructs (check paragraph 'Subcellular localization of fluorescent protein fusions'). In
600 the first step the primer pairs GFP B1 with GFP R ns BIND and GFP to TTN5 with TITAN5 stop
601 B2 were used with pABind-FRET (Bleckmann et al. 2010) as template for the fluorescent
602 protein coding sequence. The final construct was obtained with the primer pair GFP B1 with
603 TITAN5 stop B2. Constructs were cloned into pDONR207 for further cloning into pMDC7 *via*
604 LR reactions. Agrobacteria were transformed and used for *N. benthamiana* leaf infiltration.
605 FRET-APB was performed using laser-scanning confocal microscopy (LSM 780, Zeiss) with a
606 40x C-Apochromat water immersion objective. GFP was excited at 488 nm and detected at
607 491-560 nm and mCherry fluorescence was excited at 561 nm and detected at 570-633 nm.
608 GFP and mCherry channels were recorded for five scans. The mCherry signal was then
609 bleached with 70 iterations of maximum laser intensity in a specific region of interest (ROI)
610 which was set to the nucleus. Both channels were detected for additional 20 post-bleaching
611 scans. FRET-APB measurements were performed with a minimum of 10 repetitions ($n \geq 10$).

612 **Arabidopsis plant material**

613 The Arabidopsis *ttn5-1* mutant was previously described (McElver et al. 2000).
614 Heterozygous seedlings were selected by PCR on gDNA using the primer TTN5 intron1 fwd
615 and pDAP101 LB1 (Supplemental Table S1). pro35S::YFP-TTN5 and pro35S::HA_3-TTN5 lines

616 were previously described in (Mohr et al. 2024) and proIRT1::IRT1-mCitrine/*irt1-1* in (Dubeaux
617 et al. 2018). *irt1-1* (Ws) was characterized in (Vert et al. 2002) and *irt1-1* (Col-0, SALK_054554)
618 in Fukao et al. (2011).
619 Reporter lines were constructed as follows: proIRT1::IRT1-mCherry, with the mCherry at
620 position 80 in the first cytoplasmic loop, was cloned by overlap-extension PCR. *mCherry* was
621 amplified from pABind:mCherry (Bleckmann et al. 2010) using primer pair link mCh F and mCh
622 ns link R. IRT1 halves were amplified using IRT1 B1 and IRT1Q80 link R and link IRT1Q80 F
623 and IRT1 stop B2. In a last PCR IRT1-mCherry was amplified with primer pair IRT1 B1 and
624 IRT1 stop B2. BP and LR reaction (Life Technologies) were performed as described above with
625 pIM5 as destination vector. The Gateway-suitable plasmid pIM5 was created by exchanging
626 pro35S from pMCD32 with proIRT1 using AQUA cloning (Beyer et al. 2015). The IRT1 promoter
627 was amplified from gDNA using primer pair pIM5-pIRT1 F and pIM5-pIRT1 R with pMDC32-
628 complementary overhangs and the restriction sites HindIII and KpnI respectively. IRT1-GFP
629 construct, with the GFP at position 173 in the variable, cytoplasmic loop, was cloned by overlap-
630 extension PCR. *GFP* was amplified from pABind:GFP (Bleckmann et al. 2010) using primer
631 pair IG173 F and GI173 R. IRT1 halves were amplified using IRT1 B1 and IG173 R and GI173
632 R and IRT1 stop B2. In a last PCR IRT1-GFP was amplified with primer pair IRT1 B1 and IRT1
633 stop B2. BP and LR reaction were performed as described above with pMDC32 (Curtis and
634 Grossniklaus 2003) as destination vector. Agrobacterium cultures containing the plant protein
635 expression vectors, generated as described above, were used for floral dip transformation of
636 *A. thaliana*. Plants were multiplied, PCR-genotyped using specific primer pairs (Supplemental
637 Table S1) and selected according to standard procedures.

638 **Co-Immunoprecipitation experiments/pull-down**

639 Immunoprecipitation (IP) was performed with Arabidopsis seedlings grown for 10 days under
640 Fe-deficient conditions. The proIRT1::IRT1-mCherry in either HA_3-TTN5 or WT background
641 were grown and analyzed in parallel. Approximately 60 seedlings were flash-frozen in liquid
642 nitrogen. and grinded using the Retsch MM200 with cooled grinding jars in the presence of two
643 metal balls for 2 min. Grinded material was solubilized in 1 ml IP Buffer (50 mM Tris-HCl,
644 150 mM NaCl, 1 mM EDTA, 1% Triton X-100 and cOmpete Mini Protease Inhibitor, pH 8).
645 Solution was incubated for 10 min at room temperature followed by a 10 min centrifugation at
646 4°C and 17.000*g* (max. speed). The supernatant was transferred into a fresh 1.5 ml reaction
647 tube. The centrifugation step was repeated until all cellular debris were removed. 50 µl were
648 taken as Crude Extract (CE) aliquot. 25 µl anti-HA magnetic beads (Thermo Scientific, Pierce)
649 were added to the solution and reaction was incubated overnight at 4°C while rotating. A
650 magnet was used to collect the beads at the side of the reaction tube and solution was
651 transferred to a fresh 1.5 ml reaction tube (Flow through). 1 ml IP buffer was added to wash
652 beads (Wash I). Collection of the supernatant and washing procedure was repeated for a total
653 number of two washing steps. IP was performed in two replicates each (n = 2)

654 **Arabidopsis physiological Fe deficiency growth experiments**

655 Arabidopsis seeds were sterilized with sodium hypochlorite solution (6% Sodium
656 hypochlorite and 0.1% Triton X-100) and stored 24 hours at 4°C for stratification. Seedlings
657 were grown upright on Hoagland media [1.5 mM $Ca(NO_3)_2$, 0.5 mM KH_2PO_4, 1.25 mM KNO_3,
658 0.75 mM $MgSO_4$, 1.5 µM $CuSO_4$, 50 µM H_3BO_3, 50 µM KCl, 10 µM $MnSO_4$, 0.075 µM
659 $(NH_4)_6Mo_7O_{24}$, 2 µM $ZnSO_4$ and 1% sucrose, pH 5.8, supplemented with 1.4% Plant agar
660 (Duchefa)] with sufficient (50 µM FeNaEDTA, +Fe) or deficient (0 µM FeNaEDTA, -Fe) Fe

661 supply in growth chambers (CLF Plant Climatics) under long day condition (16 hours light at
662 21°C, 8 hours darkness at 19°C). Seedlings were grown on Fe-sufficient or -deficient media for
663 6 or 10 days or in a two-week growth system with plants growing 14 days on Fe-sufficient media
664 and then transferred to either fresh Fe-sufficient or Fe-deficient media for additional three days.

665 **Root length**

666 For root length comparison plants were growing for 10 days in Fe-sufficient or -deficient
667 conditions photographed including a scale in the picture. Root length were measured from root
668 tip to hypocotyl using the JMicro Vision program (Roduit, N. JMicroVision: Image analysis
669 toolbox for measuring and quantifying components of high-definition images. Version 1.3.4.
670 https://jmicrovision.github.io) (+Fe: WT n = 19; *ttn5-1* n = 28; -Fe: WT n = 16; *ttn5-1* n = 32).

671 **Chlorophyll content**

672 For chlorophyll content comparison plants were grown in the two-week system in Fe-
673 sufficient or -deficient conditions. Chlorophyll content was measured by SPAD values using
674 SPAD-502plus (Konica Minolta Optics, 2012) with up to ten biological replicates (+Fe: n = 10;
675 -Fe: n = 9). Chlorophyll content was determined in three individual experiments.

676 ***ttn5-1* phenotyping on alkaline calcareous soil**

677 Sterilized seeds were placed on Fe-sufficient Hoagland plates in three rows with 12-15
678 seeds, stratified at 4°C in darkness for three days and then (day of sowing [DAS]) grown upright
679 for nine days. Sixteen wildtype and sixteen *ttn5-1*$^{+/-}$ seedlings were selected for transfer to on
680 two soil conditions, control and alkaline calcareous soil (ACS). Control condition consisted of
681 peat-based soil (Floraton 1, Floragard, Oldenburg, Germany), 20 g vermiculite (Agrivermiculite
682 Floragard, Oldenburg, Germany) and 400 ml distilled water per liter dry soil. The ACs soil
683 additionally contained 8 g $CaCO_3$ (AppliChem, Darmstadt, Germany) and 4 g $NaHCO_3$ (Fisher
684 Scientific, Hampton, USA). The pH in water (1:10 soil:water) was 6.2 for the control soil and
685 8.0 for the ACS soil 30 minutes after mixture. The soil was filled into 7 cm*7 cm*6.5 cm pots
686 (Pöppelmann GmbH & Co. KG Kunststoffwerk–Werkzeugbau, Lohne Germany) and
687 afterwards 7.5 cm *7.5 cm large squares of ultramarine blue plotter foil (Europe Warehouse
688 GmbH & Co. KG, Wuppertal, Germany) were stuck on the pots. Seedling were then planted
689 into round holes in the foil with 1 cm diameter. Eight plants were grown per soil and condition.
690 After one week, the 1 cm large holes were closed around the seedlings.

691 Plants were watered for one week with deionised water. Then control plants were watered
692 with deionised water and ACS plants with 20 g/l $NaHCO_3$ (second week) and 25 g/l $NaHCO_3$
693 (following weeks). 28 days after sowing the plants were scanned with a MicroScan with
694 PlantEye (Phenospex, Heerlen, The Netherlands). It is a multispectral scanner determining
695 positions and color of points using a laser and four additional wavelengths (red: 624-634 nm,
696 green: 530-540 nm, blue: 465-485 nm, near-infrared: 720-750 nm). By filtering out the blue
697 color (hue 200-360) form the images the background around the plants was removed from the
698 measurements. Each plant was scanned twice and the average of the technical replicates was
699 calculated. The parameter “3D Leaf Area” and “Normalized Differential Vegetation Index”
700 (NDVI) average were determined with the PlantEye MicroScan (Phenospex, Belgium)
701 according to the instruction manual, corresponding to an approximation of aerial plant biomass
702 and chlorophyll content. Photos of the plants were acquired with a camera (α 600, Sony, Tokyo,
703 Japan).

704 **Gene expression analysis by RT-qPCR**

705 For gene expression analysis, plants were grown in the two-week system. Total RNA was
706 isolated from roots using the RNeasy Mini Kit (Qiagen) and cDNA synthesis was performed
707 with the RevertAid RT Reverse Transcription Kit (ThermoFisher Scientific). The CFX96
708 Touch™Real-Time PCR Detection System (Bio-Rad) was used for RT-qPCR performance.
709 Data processing was done with Bio-Rad CFX Manager™ (version3.1) software. Mass standard
710 curve analysis was used for determination of the absolute gene expression and the elongation
711 factor *EF1Bα* expression served as a reference for normalization. RT-qPCR was performed in
712 three biological replicates (n = 3) and two technical replicates each. All primer pairs used in this
713 study are listed in Supplemental Table S1.

714 **Fe reductase activity assay**

715 Fe reductase activity assay was performed as described in (Gratz et al. 2019). For Fe
716 reductase activity plants were grown in the two-week system in Fe-sufficient or -deficient
717 conditions. Two plants per replicate were washed in 100 mM $Ca(NO_3)_2$, then incubated for
718 1 hour in the dark in 1.5 ml Fe reductase solution (300 mM ferrozine and 100 mM FeNaEDTA).
719 The Fe reductase activity-dependent color change was measured at 562 nm using Infinite
720 200® PRO (Tecan) plate reader. Activity calculation was done using the ferrozine extinction
721 coefficient $\varepsilon = 28.6\ mM^{-1}*cm^{-1}$ and was normalized to root weight. The assay was performed
722 with a minimum of three replicates ($n \geq 3$), each consisting of a pool of two plants. Fe reductase
723 activity was determined in three individual experiments.

724 **Subcellular localization of fluorescent protein fusions and microscopy**

725 The creation of $TTN5^{T30N}$ and $TTN5^{Q70L}$ constructs by introduced point mutations and
726 generation of pro35S::YFP-TTN5 is described in Mohr et al. (2024). mCherry-tagged constructs
727 were created by overlap-extension PCR. Fluorescent protein was amplified from
728 pABind:mCherry (Bleckmann et al. 2010) using primer pair mCherry B1 and mCh R ns BIND.
729 *TTN5*, $TTN5^{T30N}$ and $TTN5^{Q70L}$ CDS were amplified with a 20 bp overlap of mCherry using mCh
730 to TTN5 and TITAN5 stop B2. In a third PCR mCherry-tagged TTN5 constructs were generated
731 with the mCherry B1 and TITAN5 stop B2 primer pair. BP and LR reaction were performed as
732 described above. As destination vector the XVE-driven β-estradiol inducible vector pMDC7
733 (Curtis and Grossniklaus 2003) was chosen. Cloning of IRT1-GFP is described above in the
734 section 'Arabidopsis plant material'. IRT1-mCherry construct is described in Ivanov et al. (2014)
735 and proIRT1::IRT1-mCitrine/*irt1-1* in Dubeaux et al. (2018). Agrobacteria were transformed
736 with the obtained constructs and tested by *N. benthamiana* leaf infiltration after two days of
737 expression.

738 Localization studies were carried out by laser-scanning confocal microscopy (LSM 780,
739 Zeiss) with a 40x C-Apochromat water immersion objective. YFP constructs were excited at
740 488 nm and detected at 491-560 nm. mCherry or FM4-64 fluorescence was excited at 561 nm
741 and detected at 570-633 nm.

742 Wortmannin (10 µM, Sigma-Aldrich) and plasma membrane dye FM4-64 (165 µM,
743 ThermoFisher Scientific) were infiltrated into *N. benthamiana* leaves. FM4-64 was detected
744 after 5 min incubation and Wortmannin was incubated for 25 min before checking the treatment
745 effect.

746 **JACoP based colocalization analysis**

747 Colocalization analysis was performed with the ImageJ (Schneider et al. 2012) Plugin Just
748 Another Colocalization Plugin (JACoP) (Bolte and Cordelières 2006). A comparison of
749 Pearson's and Overlap coefficients was done. Object-based analysis was performed for

750 spotted-structures, adapted by Ivanov et al. (2014). Percentage of colocalization for both
751 channels was calculated based on distance between geometrical centers of signals. Analysis
752 was conducted in three replicates each (n = 3).

753 **Statistical analysis**

754 One-way ANOVA was used for statistical analysis and performed in OriginPro 2019. Fisher
755 LSD or Tukey was chosen as post-hoc test with $p < 0.05$.

756 **ACCESSION NUMBERS**

757 Sequence data from this article can be found in the TAIR and GenBank data libraries under
758 accession numbers: *FRO2* (TAIR: AT1G01580), *EHB1* (TAIR: AT1G70800), *IRT1* (TAIR:
759 AT4G19690), *PATL2* (TAIR: AT1G22530), *TTN5* (TAIR: AT2G18390), and *SNX1* (TAIR:
760 AT5G06140). Raw microscopic image data are uploaded and will be available upon publication
761 of this manuscript via BioImage Archive (https://www.ebi.ac.uk/bioimage-archive/).
762

763 ## Acknowledgements

764 We thank Gintaute Matthäi and Elke Wieneke for excellent technical assistance. We thank
765 Ksenia Trofimov for microscopic help and advice, and Rubek Merina Basgaran for help with
766 protein interaction studies. We are thankful for the excellent assistance from Stefanie
767 Weidtkamp-Peters and Sebastian Hänsch, members of the Center for Advanced Imaging (CAi)
768 at the Heinrich Heine University.
769 This work was supported by the Deutsche Forschungsgemeinschaft (DFG, German Research
770 Foundation), SFB 1208 project B05 to P.B.. This work received funding by Deutsche
771 Forschungsgemeinschaft (DFG, German Research Foundation) under Germany´s Excellence
772 Strategy – EXC-2048/1 – project ID 390686111 and – TRR 341/1 - Project-ID 456082119.
773 Funding for instrumentation: Zeiss LSM780: DFG- INST 208/551-1 FUGG.
774
775
776

777 **Figure Legends**

778

779 **Figure 1. TTN5 interacts with IRT1 via the cytosolic loop and variable region IRT1vr.**

780 (A), Targeted Y2H assay between BD-IRT1vr (IRT1-variable region, vr) and AD-TTN5.
781 Yeast cotransformation samples were spotted in 10-fold dilution series ($A_{600} = 10^1$-10^4) on
782 double selective (LW; control) and triple selective +0.5 mM 3-AT (LWH, selection for protein
783 interactions) SD-plates. SNX1/SNX1, positive control (Pourcher et al. 2010), BD-IRT1vr/AD-
784 empty and BD-empty/AD-TTN5 respective negative controls. (B), Schematic representation of
785 the switching mechanism of small GTPases based on TTN5. TTN5 can switch between an
786 inactive GDP-loaded form to an active GTP-loaded one. Many small GTPases require a
787 guanidine exchange factor (GEF) for nucleotide exchange (Vernoud et al. 2003). However,
788 TTN5 has unusually high intrinsic GDP to GTP nucleotide exchange capability and help by a
789 GEF may not be needed (indicated by space between TTN5 and GEF). Nevertheless, it is not
790 excluded that TTN5 can interact with a GEF (indicated by a question mark) in plant cells. GTP
791 hydrolysis has to be catalyzed by a GTPase-activating protein (GAP) (Mohr et al. 2024). GTP-
792 loaded TTN5 can interact with effector proteins for signal transition. (C-G), Validation of TTN5-
793 IRT1vr interaction by bimolecular fluorescence complementation (BiFC) of split YFP. Proteins
794 of interest are fused either to the C- or N-terminal half of split-YFP in this assay. Potential

795 interaction is indicated by a reconstituted YFP signal. mRFP serves as a transformation control.
796 (C-E), nYFP-IRT1vr showed YFP complementation in combination with (C) cYFP-TTN5, (D)
797 cYFP-TTN5^{T30N} and cYFP-TTN5^{Q70L} variants. The complementation takes place in nucleus and
798 cytoplasm predominantly. (F-G), The combinations (F) cYFP-TTN5/nYFP-EHB1Δsig and (G)
799 cYFP-EHB1Δsig/nYFP-IRT1vr served as negative controls. Each combination was tested a
800 minimum of three times with comparable results. Scale bar 50 µm. (H-J), Confirmed interaction
801 via Förster resonance energy transfer (FRET)-acceptor photobleaching (APB). Significant
802 increase of FRET-efficiency ($FRET_E$) between IRT1vr-mCherry (IRT1vr-mC) and (H) GFP-
803 TTN5 (G-TTN5), (I) GFP-TTN5^{T30N} (G-TTN5^{T30N}) or (J) GFP-TTN5^{Q70L} (G-TTN5^{Q70L}) indicate
804 short protein distances. GFP-fusions are donor-only samples and serve as a negative control.
805 GFP-mCherry-tagged constructs show intra-molecular FRET as a respective positive control.
806 Each combination was tested a minimum of three times with comparable results with a
807 minimum of ten individual measurements ($n \geq 10$). The box represents the 25–75th percentiles,
808 and the median is indicated. The whiskers show the 5th and 95th percentiles. One-way ANOVA
809 with Tukey post-hoc test was performed. Different letters indicate statistical significance
810 ($p < 0.05$). (K) *In planta* coimmunoprecipitation (Co-IP) experiment demonstrating interaction
811 between full-length IRT1-mCherry (proIRT1::IRT1Q80-mCherry) and HA_3-TTN5 (pro35S::HA_3-
812 TTN5) using Arabidopsis roots carrying both transgenes or only IRT1-mCherry grown in parallel
813 under Fe-deficient conditions. Following protein complex extraction, coimmunoprecipitation
814 was conducted with anti-HA antibody. HA_3-TTN5 protein was enriched by the pull-down,
815 resulting in an increased band intensity in the elution (IP) fraction compared to the input.
816 IRT1Q80-mCherry protein was copurified with HA_3-TTN5 in two out of three repetitions. No
817 coimmunoprecipitation is detected in the negative control in the absence of HA_3-TTN5 protein.
818

819 **Figure 2. Heterozygous *ttn5-1*$^{+/-}$ seedlings can have an Fe reductase phenotype.**
820 Heterozygous *ttn5-1*$^{+/-}$ and their wild type sibling seedlings were grown on +/-Fe
821 Hoagland plates for ten days (A, B) or in the two-week system (C-H). All plants were individually
822 genotyped as wild type or *ttn5-1*$^{+/-}$. Note that homozygous *ttn5-1*$^{+/+}$ are embryo-lethal. (A), +
823 and -Fe-grown *ttn5-1*$^{+/-}$ seedlings appeared phenotypically as wild type (WT) siblings. Scale
824 bar 1 cm. (B), Quantified root length of (A). Root length increased under Fe-deficient conditions
825 (-Fe, light grey boxes) compared to sufficient conditions (+Fe, dark grey boxes), similar in *ttn5-*
826 *1*$^{+/-}$ and wild type siblings (+Fe: WT n = 19; *ttn5-1*$^{+/-}$ n = 28; -Fe: WT n = 16; *ttn5-1*$^{+/-}$ n = 32).
827 The box represents the 25–75th percentiles, and the median is indicated. The whiskers show
828 the 5th and 95th percentiles. (C), Soil Plant Analysis Development (SPAD) values, reflecting
829 chlorophyll amounts, were similar under both Fe conditions (-Fe, light grey boxes; +Fe, dark
830 grey boxes) and comparable between the plants (+Fe: n = 10; -Fe: n = 9). The box represents
831 the 25–75th percentiles, and the median is indicated. The whiskers show the 5th and 95th
832 percentiles. (D-F), Gene expression data determined by RT-qPCR of *TTN5, FRO2* and *IRT1*
833 in *ttn5-1*$^{+/-}$ roots compared to wild type siblings in Fe-sufficient (+Fe, black bars) or -deficient (-
834 Fe, grey bars) conditions. (D), *TTN5* expression levels were higher in +Fe than -Fe conditions
835 in wild type and *ttn5-1*$^{+/-}$ seedlings. Expression was about half in mutant versus wild type (E-F)
836 *FRO2* and *IRT1* expression was induced upon Fe deficiency versus sufficiency in wild type and
837 *ttn5-1*$^{+/-}$ seedlings in comparable amounts. Data was obtained from three biological replicates
838 (n = 3). (G), Root ferric reductase activity determined by the Fe^{2+}-ferrozine assay at 562 nm.
839 Iron reductase activity was increased upon Fe deficiency in wild type. Same was found in *ttn5-*
840 *1*$^{+/-}$ sibling seedlings under Fe deficiency but to lesser extent. The assay was performed with

three (wild type) and four (*ttn5-1*$^{+/-}$) biological replicates (WT n = 3; *ttn5-1*$^{+/-}$ n = 4). The experiment was repeated in total three times. In two cases, Fe reductase activity was reduced in *ttn5-1*$^{+/-}$ compared with wild type siblings (one representative experiment shown), and once it was not different. One-way ANOVA with Tukey as post-hoc test was performed. Different letters indicate statistical significance ($p < 0.05$).

Figure 3. TTN5 and IRT1 fluorescence protein signals colocalize at the plasma membrane and in multi-vesicular bodies (MVBs) in *N. benthamiana* leaf pavement cells.

Fluorescent signals of mCherry-TTN5 and its mutant derivatives mCherry-TTN5^{T30N} and mCherry-TTN5^{Q70L} were colocalized with IRT1-GFP (pro35S::IRT1-GFP) expression in *N. benthamiana* leaf pavement cells. (A-C), Fluorescent signals of mCherry-TTN5 and mCherry-TTN5 variants expressing constructs were present at the plasma membrane and in distinct spots together with IRT1-GFP signal. (D), JACoP-based colocalization analysis of mCherry-TTN5 and variants with IRT1-GFP (Bolte and Cordelières, 2006) performed with ImageJ (Schneider et al. 2012). Comparison of Pearson's coefficients for IRT1-GFP with mCherry-TTN5, mCherry-TTN5^{T30N} and mCherry-TTN5^{Q70L} at the plasma membrane (PM). Fluorescent signals of mCherry-TTN5^{T30N} construct were statistically significant more present at the PM compared to signals of mCherry-TTN5 and mCherry-TTN5^{Q70L}. (E-G), Internalized fluorescent signals of IRT1-GFP expression were present in vesicle-like structures positively labelled by mCherry-TTN5 and mCherry-TTN5 variant signals. (H), Comparison of Pearson's coefficients for IRT1-GFP with mCherry-TTN5, mCherry-TTN5^{T30N} and mCherry-TTN5^{Q70L} in internalized spots. Fluorescent signals of all mCherry-TTN5 construct colocalized in a similar way with IRT1-GFP signals. (I), Schematic illustration of the inhibiting function of the fungal metabolite wortmannin on cellular trafficking routes between the vacuole and the *trans*-Golgi network via MVBs, leading to swelling of MVBs. (J-L), Cells were treated with wortmannin (10 µM). Swollen MVBs are visible with the GFP- and mCherry-channel, respectively. Colocalization is indicated with filled arrowheads. Microscopic experiments were conducted in a minimum of three repetitions ($n \geq 3$). JACoP analyses were performed three times ($n = 3$). One-way ANOVA with Fisher-LSD as post-hoc test was performed. Different letters indicate statistical significance ($p < 0.05$). Scale bar 10 µm.

Figure 4. TTN5 interacts with IRT1 regulators EHB1, SNX1 and PATL2.

(A-E, G-P), Bimolecular fluorescence complementation (BiFC) of split YFP experiments with TTN5 and known IRT1 regulators EHB1 (Khan et al. 2019), SNX1 (Ivanov et al. 2014) and PATL2 (Hornbergs et al. 2023). mRFP expression serves as a transformation control. (A-E), TTN5 interacts with EHB1 via the sig domain. (B) TTN5 and EHB1 showed complementation whereas (D, E) variants were not able to complement split-YFP. (A, C) TTN5 was tested together with EHB1sig (signature domain, sig domain only) and with EHB1 harboring a deletion of the CAR sig domain (sig domain defined in Rodriguez et al. (2014), Khan et al. (2019), EHB1Δsig). Deletion of the sig domain resulted in loss of complementation. (F), Interaction between EHB1-GFP (donor) with TTN5-mCherry and TTN5-mCherry variants (acceptor) was confirmed by FRET-APB. EHB1-GFP as donor-only sample (negative control), EHB1-GFP-mCherry for intra-molecular FRET (positive control). In this assay, TTN5 variants interacted with EHB1. Each combination was tested a minimum of three times with a minimum of ten individual measurements ($n \geq 10$) with comparable results. The box represents the 25–75th

886 percentiles, and the median is indicated. The whiskers show the 5th and 95th percentiles. (G-
887 K), BiFC showing that TTN5 interacts with SNX1. (G) TTN5 and (I) TTN5^{Q70L} showed
888 complemented YFP signal together with SNX1. No YFP fluorescence was detectable for (H)
889 TTN5^{T30N} with SNX1. (J, K), An interaction took place between TTN5 and the (J) PX and (K)
890 the BAR domain of SNX1. (L-P), BiFC showing that TTN5 interacted with PATL2. (L) PATL2
891 showed complemented YFP signal with N-terminally-tagged TTN5. (M) TTN5^{T30N} and (N)
892 TTN5^{Q70L} did not complement YFP with PATL2. (O-P), Deletion mutants of PATL2 showed
893 dependency of the N-terminus for complementation with TTN5. (O) YFP signal was visible for
894 PATL2 N-terminus (PATL2ΔC). (P) On the other hand, the C-terminus alone (PATL2ΔN) had
895 no detectable YFP. Every construct was tested a minimum of three times ($n \geq 3$) with similar
896 results. Scale bar 50 µm. One-way ANOVA with Tukey post-hoc test was performed. Different
897 letters indicate statistical significance ($p < 0.05$).
898

899 **Figure 5. Summary model: Action of TTN5 within the IRT1-regulatory network.**
900 A schematic overview of the identified TTN5 interactors within the IRT1-regulatory
901 network (A) at the plasma membrane (PM) or (B) in the endomembrane compartments of the
902 *trans*-Golgi network (TGN) or multivesicular body (MVB). IRT1 undergoes a constant cycling
903 due to endocytosis from the plasma membrane and either degradation via the lytic pathway in
904 the vacuole or recycling back to the plasma membrane. (A), We identified TTN5 interaction
905 with the large cytosolic, variable region of IRT1. TTN5 and IRT1 colocalized at the plasma
906 membrane (1). PATL2 interacts with the large cytosolic, variable region of IRT1 (IRT1vr) via its
907 N-terminus and may be involved in α-tocopherol recruitment to the membrane, to prevent lipid
908 peroxidation induced by IRT1-related Fe import (Hornbergs et al. 2023). TTN5 also interacts
909 with the N-terminus of PATL2. A potential TTN5-PATL2-IRT1 complex formation is suggested
910 (2). EHB1 interacts with the large cytosolic, variable region of IRT1 via its signature (sig) domain
911 and inhibits IRT1 function at the plasma membrane in a Ca^{2+}-dependent manner (Khan et al.
912 2019). TTN5 also interacted with EHB1 via the sig domain. A potential TTN5-EHB1-IRT1
913 complex formation is suggested (3). A possible quadruple complex of IRT1, TTN5, PATL2 and
914 EHB1 (4). (B) We found that IRT1 colocalized with SNX1 (Ivanov et al. 2014) and TTN5 in the
915 TGN. IRT1 and TTN5 also colocalized in MVBs. The protein representations are explained in
916 the legend, a potential protein complex that may form, is indicated by a question mark.
917

918 **Supplemental Figure S1. IRT1Q80-mCherry complements *irt1-1* knockout phenotypes.**
919 Complementation of the rosette growth defect, leaf chlorosis and reproductive capacity of *irt1-*
920 *1* (SALK_054554) by IRT1-mCherry. Seedlings of wild type (WT), proIRT1::IRT1-mCherry/*irt1-*
921 *1* (briefly IRT1-mCherry) and *irt1-1* were grown on soil. Rosettes were imaged after 20, 28 and
922 49 days. IRT1-mCherry lines complemented both the defect in rosette growth, leaf chlorosis,
923 and silique formation of the *irt1-1* mutant and were comparable to the wild type. Scale bar
924 horizontal: 1 cm, vertical: 5 cm.

925

926 **Supplemental Figure S2. Alkaline calcareous soil similarly impacts growth of *ttn5-1*$^{+/-}$**
927 **and wild type plants.**
928 Heterozygous *ttn5-1*$^{+/-}$ and their wild type sibling seedlings were grown in comparison
929 on +Fe Hoagland plates for 9 days and then transferred to alkaline, calcareous soil (ACS) or
930 control conditions. Phenotypical analysis was conducted 15, 23, 28, 35 and 43 days after

931 sowing using PlantEye (Phenospex). (A), Growth of wild type (WT; dark colors) and *ttn5-1*$^{+/-}$
932 (bright colors) plants on both, control (circle) and ACS (triangle) soil conditions determined by
933 3D leaf area. The parameter "3D Leaf Area" represents the area of the surface of the whole
934 scanned object visible from straight above, including rosettes, stems and inflorescences. ACS
935 condition led to a reduced 3D leaf area for both wild type and *ttn5-1*$^{+/-}$. (B-D), Detailed
936 phenotypical analysis of WT and *ttn5-1*$^{+/-}$ after 23 days. (B) Images of WT and *ttn5-1*$^{+/-}$ on both
937 soil conditions. ACS condition led to a reduced rosette size for both. Scale bar 1 cm. (C),
938 PlantEye analysis confirmed a significant reduced 3D leaf area on ACS compared to control
939 conditions for both wild type (WT) and *ttn5-1*$^{+/-}$ plants in a similar amount. The box represents
940 the 25–75th percentiles, and the median is indicated. The whiskers show the 5th and 95th
941 percentiles. (D), Normalized difference vegetation index (NDVI) was used as a correlation
942 factor for photosynthetic efficiency. For the NDVI, the reflectance of red (RED, 624-634 nm)
943 and near-infrared (NIR, 720-750 nm) light is determined at all points of the scanned object, that
944 are reached by the light. The NDVI is then calculated as (NIR – RED) / (NIR + RED) for each
945 point and the average over the object is determined. WT plants grown in ACS condition had a
946 significant reduced NDVI compared to control soil while this effect was less the case for *ttn5-*
947 *1*$^{+/-}$ plants. The experiment was performed with eight biological replicates (n = 8). The box
948 represents the 25–75th percentiles, and the median is indicated. The whiskers show the 5th and
949 95th percentiles. One-way ANOVA with Tukey post-hoc test was performed. Different letters
950 indicate statistical significance ($p < 0.05$).
951
952 **Supplemental Figure S3. Localization of IRT1 and TTN5 fluorescence fusion proteins in**
953 **the Arabidopsis root elongation zone.**
954 (A, C, E) IRT1-mCitrine localization in proIRT1::IRT1-mCitrine/*irt1-1* seedling roots (line
955 previously described in Dubeaux et al. (2018), Hornbergs et al. (2023)) in comparison with (B,
956 D, F) YFP-TTN5 localization in pro35S::YFP-TTN5/WT seedling roots (line previously
957 described in Mohr et al. (2024)) in the root elongation zone. Plants were grown on plates side
958 by side. (A, B), Longitudinal confocal sections through the stele. (A) IRT1-mCitrine was present
959 at the plasma membrane of epidermal cells (empty white arrowhead). (B) Fluorescent signal of
960 YFP-TTN5 roots was localized at the plasma membrane of epidermal cells and other cell types,
961 as well as in the stele (empty magenta arrowhead). Dotted white lines indicate the position of
962 the cross sections shown in C and D. (C-D), Cross confocal sections highlighting (C) IRT1-
963 mCitrine in epidermal cells compared to (D) nearly ubiquitously localized fluorescent signal in
964 YFP-TTN5 roots. (E-F), Longitudinal section through the epidermis regions. Next to plasma
965 membrane, (E) IRT1-mCitrine and (F) YFP-TTN5 were present in intracellular spots (filled white
966 arrowheads). YFP-TTN5 was also detected in the nucleus (filled magenta arrowhead). The
967 experiment was repeated in a minimum of three times ($n \geq 3$). Scale bar 10 µm.
968
969 **Supplemental Figure S4. IRT1 colocalization analysis at the plasma membrane and in**
970 **intracellular spots.**
971 (A), Plasma membrane dye FM4-64 indicated IRT1-GFP localization at the plasma
972 membrane. IRT1-GFP is present in a spotted structure, indicating regions of higher transporter
973 accumulation. (B-C), IRT1-GFP colocalized with IRT1-mCherry (Ivanov et al. 2014) (B) at the
974 plasma membrane (PM) and (C) in swollen intracellular spots after wortmannin treatment
975 (10 µM), confirming correct localization of IRT1-GFP. The experiments were repeated in a
976 minimum of three times ($n \geq 3$). Scale bar 50 µm. (D), Complementation of rosette growth

977 defect of *irt1-1* by IRT1-GFP. Rosette sizes of *irt1-1* and pro35S::IRT1-GFP/*irt1-1* were
978 measured 14 days after sowing. IRT1-GFP complemented the growth defect of *irt1-1*. The
979 experiment was conducted once with twelve biological replicates (n = 12). The box represents
980 the 25–75th percentiles, and the median is indicated. The whiskers show the 5th and 95th
981 percentiles. (E-G), JACoP-based colocalization analysis of mCherry-TTN5 and variants with
982 IRT1-GFP (Bolte and Cordelières, 2006) performed with ImageJ (Schneider et al. 2012). See
983 also Figure 3A-H. (E-F), Comparison of (from left to right) Overlap coefficients for IRT1-GFP
984 with mCherry-TTN5, mCherry-TTN5^{T30N} and mCherry-TTN5^{Q70L} (E) at the plasma membrane
985 and (F) in vesicle-like structures. (G), Object-based analysis was performed for spotted-
986 structures based on distance between geometrical centers of signals. Analyses were
987 conducted in three replicates each (n = 3). One-way ANOVA with Fisher-LSD post-hoc test
988 was performed. Different letters indicate statistical significance ($p < 0.05$).
989
990 **Supplemental Figure S5. Gene expression of *EHB1*, *SNX1* and *PATL2* is not affected in**
991 ***ttn5-1$^{+/-}$* plants.**
992 Gene expression data by RT-qPCR of *EHB1*, *SNX1* and *PATL2* in *ttn5-1$^{+/-}$* roots
993 compared to wild type sibling roots. Plants were grown in the two-week system in Fe-sufficient
994 (+Fe, black bars) or -deficient (-Fe, grey bars) conditions. See also Figure 2D-F. (A), *EHB1*
995 expression was down-regulated under Fe-deficient conditions in wild type seedlings, while
996 expression levels were not differing in *ttn5-1$^{+/-}$* seedlings under both Fe supply conditions. (B),
997 *SNX1* expression was not altered between Fe-sufficient or -deficient conditions in wild type and
998 *ttn5-1$^{+/-}$*seedlings. (C), *PATL2* expression did not change upon Fe supply in both wild type and
999 *ttn5-1$^{+/-}$*seedlings. Data were obtained from three biological replicates (n = 3). One-way ANOVA
1000 with Fisher-LSD post-hoc test was performed. Different letters indicate statistical significance
1001 ($p < 0.05$).
1002
1003 **Supplemental Table S1: Primer list**
1004
1005 **References**
1006 **Adarska, P., L. Wong-Dilworth and F. Bottanelli** (2021). "ARF GTPases and Their
1007 Ubiquitous Role in Intracellular Trafficking Beyond the Golgi." Frontiers in cell and
1008 developmental biology **9**: 679046-679046.
1009 **Anders, N., M. Nielsen, J. Keicher, Y. D. Stierhof, M. Furutani, M. Tasaka, K. Skriver and**
1010 **G. Jürgens** (2008). "Membrane association of the Arabidopsis ARF exchange factor GNOM
1011 involves interaction of conserved domains." Plant Cell **20**(1): 142-151.
1012 **Antoshechkin, I. and M. Han** (2002). "The *C. elegans* evl-20 Gene Is a Homolog of the Small
1013 GTPase ARL2 and Regulates Cytoskeleton Dynamics during Cytokinesis and Morphogenesis."
1014 Developmental Cell **2**(5): 579-591.
1015 **Arora, D. and D. Van Damme** (2021). "Motif-based endomembrane trafficking." Plant
1016 Physiology **186**(1): 221-238.
1017 **Barberon, M., G. Dubeaux, C. Kolb, E. Isono, E. Zelazny and G. Vert** (2014). "Polarization
1018 of IRON-REGULATED TRANSPORTER 1 (IRT1) to the plant-soil interface plays crucial role in
1019 metal homeostasis." Proceedings of the National Academy of Sciences **111**(22): 8293-8298.
1020 **Barberon, M., E. Zelazny, S. Robert, G. Conéjéro, C. Curie, J. Friml and G. Vert** (2011).
1021 "Monoubiquitin-dependent endocytosis of the IRON-REGULATED TRANSPORTER 1 (IRT1)
1022 transporter controls iron uptake in plants." Proceedings of the National Academy of Sciences
1023 **108**(32): E450-E458.

Benková, E., M. Michniewicz, M. Sauer, T. Teichmann, D. Seifertová, G. Jürgens and J. Friml (2003). "Local, Efflux-Dependent Auxin Gradients as a Common Module for Plant Organ Formation." Cell **115**(5): 591-602.

Beyer, H. M., P. Gonschorek, S. L. Samodelov, M. Meier, W. Weber and M. D. Zurbriggen (2015). "AQUA Cloning: A Versatile and Simple Enzyme-Free Cloning Approach." PLoS One **10**(9): e0137652.

Bhamidipati, A., S. A. Lewis and N. J. Cowan (2000). "ADP ribosylation factor-like protein 2 (Arl2) regulates the interaction of tubulin-folding cofactor D with native tubulin." Journal of Cell Biology **149**(5): 1087-1096.

Bleckmann, A., S. Weidtkamp-Peters, C. A. M. Seidel and R. Simon (2010). "Stem cell signaling in Arabidopsis requires CRN to localize CLV2 to the plasma membrane." Plant physiology **152**(1): 166-176.

Bolte, S. and F. P. Cordelières (2006). "A guided tour into subcellular colocalization analysis in light microscopy." J Microsc **224**(Pt 3): 213-232.

Chen, W., H. Zhou, F. Xu, M. Yu, A. Coego, L. Rodriguez, Y. Lu, Q. Xie, Q. Fu, J. Chen, G. Xu, D. Wu, X. Li, X. Li, Y. Jaillais, P. L. Rodriguez, S. Zhu and F. Yu (2023). "CAR modulates plasma membrane nano-organization and immune signaling downstream of RALF1-FERONIA signaling pathway." New Phytol **237**(6): 2148-2162.

Cointry, V. and G. Vert (2019). "The bifunctional transporter-receptor IRT1 at the heart of metal sensing and signalling." New Phytologist **223**(3): 1173-1178.

Connolly, E. L., J. P. Fett and M. L. Guerinot (2002). "Expression of the IRT1 metal transporter is controlled by metals at the levels of transcript and protein accumulation." Plant Cell **14**(6): 1347-1357.

Cui, M. G., S.K. and P. Bauer (2023). "Review: Role of the plant-specific calcium-binding C2-DOMAIN ABSCISIC ACID-RELATED (CAR) protein family in environmental signaling. ." OSF Preprints.

Cui, Y., X. Li, Q. Chen, X. He, Q. Yang, A. Zhang, X. Yu, H. Chen, N. Liu, Q. Xie, W. Yang, J. Zuo, K. Palme and W. Li (2010). "BLOS1, a putative BLOC-1 subunit, interacts with SNX1 and modulates root growth in Arabidopsis." Journal of Cell Science **123**(21): 3727-3733.

Cui, Y., J. Shen, C. Gao, X. Zhuang, J. Wang and L. Jiang (2016). "Biogenesis of Plant Prevacuolar Multivesicular Bodies." Molecular Plant **9**(6): 774-786.

Curtis, M. D. and U. Grossniklaus (2003). "A gateway cloning vector set for high-throughput functional analysis of genes in planta." Plant physiology **133**(2): 462-469.

Dubeaux, G., J. Neveu, E. Zelazny and G. Vert (2018). "Metal Sensing by the IRT1 Transporter-Receptor Orchestrates Its Own Degradation and Plant Metal Nutrition." Molecular Cell **69**(6): 953-964.e955.

Dümmer, M., C. Michalski, L. O. Essen, M. Rath, P. Galland and C. Forreiter (2016). "EHB1 and AGD12, two calcium-dependent proteins affect gravitropism antagonistically in *Arabidopsis thaliana*." J Plant Physiol **206**: 114-124.

Eide, D., M. Broderius, J. Fett and M. L. Guerinot (1996). "A novel iron-regulated metal transporter from plants identified by functional expression in yeast." Proceedings of the National Academy of Sciences of the United States of America **93**(11): 5624-5628.

Fansa, E. K. and A. Wittinghofer (2016). "Sorting of lipidated cargo by the Arl2/Arl3 system." Small GTPases **7**(4): 222-230.

Fleming, J. A., L. R. Vega and F. Solomon (2000). "Function of tubulin binding proteins in vivo." Genetics **156**(1): 69-80.

Francis, J. W., R. E. Turn, L. E. Newman, C. Schiavon and R. A. Kahn (2016). "Higher order signaling: ARL2 as regulator of both mitochondrial fusion and microtubule dynamics allows integration of 2 essential cell functions." Small GTPases **7**(4): 188-196.

Frost, A., V. M. Unger and P. De Camilli (2009). "The BAR Domain Superfamily: Membrane-Molding Macromolecules." Cell **137**(2): 191-196.

Fukao, Y., A. Ferjani, R. Tomioka, N. Nagasaki, R. Kurata, Y. Nishimori, M. Fujiwara and M. Maeshima (2011). "iTRAQ Analysis Reveals Mechanisms of Growth Defects Due to Excess Zinc in Arabidopsis " Plant Physiology **155**(4): 1893-1907.

Fukaya, M., D. Fukushima, Y. Hara and H. Sakagami (2014). "EFA6A, a guanine nucleotide exchange factor for Arf6, interacts with sorting nexin-1 and regulates neurite outgrowth." Journal of Neurochemistry **129**(1): 21-36.

Gaither, L. A. and D. J. Eide (2001). "Eukaryotic zinc transporters and their regulation." Biometals **14**(3-4): 251-270.

Geldner, N., N. Anders, H. Wolters, J. Keicher, W. Kornberger, P. Muller, A. Delbarre, T. Ueda, A. Nakano and G. Jürgens (2003). "The Arabidopsis GNOM ARF-GEF mediates endosomal recycling, auxin transport, and auxin-dependent plant growth." Cell **112**(2): 219-230.

Gratz, R., P. Manishankar, R. Ivanov, P. Köster, I. Mohr, K. Trofimov, L. Steinhorst, J. Meiser, H. J. Mai, M. Drerup, S. Arendt, M. Holtkamp, U. Karst, J. Kudla, P. Bauer and T. Brumbarova (2019). "CIPK11-Dependent Phosphorylation Modulates FIT Activity to Promote Arabidopsis Iron Acquisition in Response to Calcium Signaling." Dev Cell **48**(5): 726-740.e710.

Gratz, R., C. von der Mark, R. Ivanov and T. Brumbarova (2021). "Fe acquisition at the crossroad of calcium and reactive oxygen species signaling." Curr Opin Plant Biol **63**: 102048.

Grefen, C. and M. R. Blatt (2012). "A 2in1 cloning system enables ratiometric bimolecular fluorescence complementation (rBiFC)." Biotechniques **53**(5): 311-314.

Grossoehme, N. E., S. Akilesh, M. L. Guerinot and D. E. Wilcox (2006). "Metal-Binding Thermodynamics of the Histidine-Rich Sequence from the Metal-Transport Protein IRT1 of *Arabidopsis thaliana*." Inorganic Chemistry **45**(21): 8500-8508.

Guerinot, M. L. (2000). "The ZIP family of metal transporters." Biochimica et Biophysica Acta (BBA) - Biomembranes **1465**(1): 190-198.

Heucken, N. and R. Ivanov (2018). "The retromer, sorting nexins and the plant endomembrane protein trafficking." J Cell Sci **131**(2).

Hornbergs, J., K. Montag, J. Loschwitz, I. Mohr, G. Poschmann, A. Schnake, R. Gratz, T. Brumbarova, M. Eutebach, K. Angrand, C. Fink-Straube, K. Stühler, J. Zeier, L. Hartmann, B. Strodel, R. Ivanov and P. Bauer (2023). "SEC14-GOLD protein PATELLIN2 binds IRON-REGULATED TRANSPORTER1 linking root iron uptake to vitamin E." Plant Physiol **192**(1): 504-526.

Hu, J. (2021). "Toward unzipping the ZIP metal transporters: structure, evolution, and implications on drug discovery against cancer." The FEBS Journal **288**(20): 5805-5825.

Ismail, S. A., Y. X. Chen, A. Rusinova, A. Chandra, M. Bierbaum, L. Gremer, G. Triola, H. Waldmann, P. I. Bastiaens and A. Wittinghofer (2011). "Arl2-GTP and Arl3-GTP regulate a GDI-like transport system for farnesylated cargo." Nat Chem Biol **7**(12): 942-949.

Ismail, S. A., I. R. Vetter, B. Sot and A. Wittinghofer (2010). "The Structure of an Arf-ArfGAP Complex Reveals a Ca^{2+} Regulatory Mechanism." Cell **141**(5): 812-821.

Ivanov, R., T. Brumbarova, A. Blum, A.-M. Jantke, C. Fink-Straube and P. Bauer (2014). "SORTING NEXIN1 is required for modulating the trafficking and stability of the Arabidopsis IRON-REGULATED TRANSPORTER1." The Plant cell **26**(3): 1294-1307.

Ivanov, R. and G. Vert (2021). "Endocytosis in plants: Peculiarities and roles in the regulated trafficking of plant metal transporters." Biology of the Cell **113**(1): 1-13.

Jaillais, Y., I. Fobis-Loisy, C. Miège, C. Rollin and T. Gaude (2006). "AtSNX1 defines an endosome for auxin-carrier trafficking in Arabidopsis." Nature **443**(7107): 106-109.

Kerkeb, L., I. Mukherjee, I. Chatterjee, B. Lahner, D. E. Salt and E. L. Connolly (2008). "Iron-induced turnover of the Arabidopsis IRON-REGULATED TRANSPORTER1 metal transporter requires lysine residues." Plant physiology **146**(4): 1964-1973.

Khan, I., R. Gratz, P. Denezhkin, S. N. Schott-Verdugo, K. Angrand, L. Genders, R. M. Basgaran, C. Fink-Straube, T. Brumbarova, H. Gohlke, P. Bauer and R. Ivanov (2019). "Calcium-Promoted Interaction between the C2-Domain Protein EHB1 and Metal Transporter IRT1 Inhibits Arabidopsis Iron Acquisition." Plant Physiology **180**(3): 1564-1581.

Kleine-Vehn, J., P. Dhonukshe, M. Sauer, P. B. Brewer, J. Wiśniewska, T. Paciorek, E. Benková and J. Friml (2008). "ARF GEF-dependent transcytosis and polar delivery of PIN auxin carriers in Arabidopsis." Curr Biol **18**(7): 526-531.

Knauer, T., M. Dümmer, F. Landgraf and C. Forreiter (2011). "A negative effector of blue light-induced and gravitropic bending in Arabidopsis." Plant physiology **156**(1): 439-447.

Kolb, C., M.-K. Nagel, K. Kalinowska, J. Hagmann, M. Ichikawa, F. Anzenberger, A. Alkofer, M. H. Sato, P. Braun and E. Isono (2015). "FYVE1 is essential for vacuole biogenesis and intracellular trafficking in Arabidopsis." Plant physiology **167**(4): 1361-1373.

Le, C. T. T., T. Brumbarova, R. Ivanov, C. Stoof, E. Weber, J. Mohrbacher, C. Fink-Straube and P. Bauer (2015). "ZINC FINGER OF ARABIDOPSIS THALIANA12 (ZAT12) Interacts with FER-LIKE IRON DEFICIENCY-INDUCED TRANSCRIPTION FACTOR (FIT) Linking Iron Deficiency and Oxidative Stress Responses " Plant Physiology **170**(1): 540-557.

Li, W., Y. Feng, C. Hao, X. Guo, Y. Cui, M. He and X. He (2007). "The BLOC Interactomes Form a Network in Endosomal Transport." Journal of Genetics and Genomics **34**(8): 669-682.

Martín-Barranco, A., J. Spielmann, G. Dubeaux, G. Vert and E. Zelazny (2020). "Dynamic Control of the High-Affinity Iron Uptake Complex in Root Epidermal Cells1." Plant Physiology **184**(3): 1236-1250.

Mayer, U., U. Herzog, F. Berger, D. Inzé and G. Jürgens (1999). "Mutations in the PILZ group genes disrupt the microtubule cytoskeleton and uncouple cell cycle progression from cell division in Arabidopsis embryo and endosperm." European Journal of Cell Biology **78**(2): 100-108.

McElver, J., D. Patton, M. Rumbaugh, C.-m. Liu, L. J. Yang and D. Meinke (2000). "The TITAN5 Gene of Arabidopsis Encodes a Protein Related to the ADP Ribosylation Factor Family of GTP Binding Proteins." The Plant Cell **12**(8): 1379-1392.

Memon, A. R. (2004). "The role of ADP-ribosylation factor and SAR1 in vesicular trafficking in plants." Biochim Biophys Acta **1664**(1): 9-30.

Mohr, I., A. Mirzaiebadizi, S. K. Sanyal, P. Chuenban, M. R. Ahmadian, R. Ivanov and P. Bauer (2024). "Characterization of the small Arabidopsis thaliana GTPase and ADP-ribosylation factor-like 2 protein TITAN 5." Journal of Cell Science.

Montag, K., J. Hornbergs, R. Ivanov and P. Bauer (2020). "Phylogenetic analysis of plant multi-domain SEC14-like phosphatidylinositol transfer proteins and structure–function properties of PATELLIN2." Plant Molecular Biology **104**(6): 665-678.

Montag, K., R. Ivanov and P. Bauer (2023). "Role of SEC14-like phosphatidylinositol transfer proteins in membrane identity and dynamics." OSF Preprints.

Mori, R. and T. Toda (2013). "The dual role of fission yeast Tbc1/cofactor C orchestrates microtubule homeostasis in tubulin folding and acts as a GAP for GTPase Alp41/Arl2." Mol Biol Cell **24**(11): 1713-1724, s1711-1718.

Nielsen, E. (2020). "The Small GTPase Superfamily in Plants: A Conserved Regulatory Module with Novel Functions." Annual Review of Plant Biology **71**(1): 247-272.

Ohwaki, Y. and K. Sugahara (1997). "Active extrusion of protons and exudation of carboxylic acids in response to iron deficiency by roots of chickpea (Cicer arietinum L.)." Plant and Soil **189**(1): 49-55.

Peter, B. J., H. M. Kent, I. G. Mills, Y. Vallis, P. J. Butler, P. R. Evans and H. T. McMahon (2004). "BAR domains as sensors of membrane curvature: the amphiphysin BAR structure." Science **303**(5657): 495-499.

Pourcher, M., M. Santambrogio, N. Thazar, A.-M. Thierry, I. Fobis-Loisy, C. Miège, Y. Jaillais and T. Gaude (2010). "Analyses of sorting nexins reveal distinct retromer-subcomplex functions in development and protein sorting in *Arabidopsis thaliana*." The Plant cell **22**(12): 3980-3991.

Radcliffe, P. A., L. Vardy and T. Toda (2000). "A conserved small GTP-binding protein Alp41 is essential for the cofactor-dependent biogenesis of microtubules in fission yeast." FEBS Letters **468**(1): 84-88.

Raposo, G., M. S. Marks and D. F. Cutler (2007). "Lysosome-related organelles: driving post-Golgi compartments into specialisation." Current Opinion in Cell Biology **19**(4): 394-401.

Rath, M., M. Dümmer, P. Galland and C. Forreiter (2020). "A gravitropic stimulus alters the distribution of EHB1, a negative effector of root gravitropism in Arabidopsis." Plant Direct **4**(4): e00215.

Robinson, N. J., C. M. Procter, E. L. Connolly and M. L. Guerinot (1999). "A ferric-chelate reductase for iron uptake from soils." Nature **397**(6721): 694-697.

Rodriguez, L., M. Gonzalez-Guzman, M. Diaz, A. Rodrigues, A. C. Izquierdo-Garcia, M. Peirats-Llobet, M. A. Fernandez, R. Antoni, D. Fernandez, J. A. Marquez, J. M. Mulet, A. Albert and P. L. Rodriguez (2014). "C2-domain abscisic acid-related proteins mediate the interaction of PYR/PYL/RCAR abscisic acid receptors with the plasma membrane and regulate abscisic acid sensitivity in Arabidopsis." Plant Cell **26**(12): 4802-4820.

Schmid, N. B., R. F. Giehl, S. Döll, H. P. Mock, N. Strehmel, D. Scheel, X. Kong, R. C. Hider and N. von Wirén (2014). "Feruloyl-CoA 6'-Hydroxylase1-dependent coumarins mediate iron acquisition from alkaline substrates in Arabidopsis." Plant Physiol **164**(1): 160-172.

Schneider, C. A., W. S. Rasband and K. W. Eliceiri (2012). "NIH Image to ImageJ: 25 years of image analysis." Nature Methods **9**(7): 671-675.

Sharer, J. D., J. F. Shern, H. Van Valkenburgh, D. C. Wallace and R. A. Kahn (2002). "ARL2 and BART Enter Mitochondria and Bind the Adenine Nucleotide Transporter." Molecular Biology of the Cell **13**(1): 71-83.

Shin, L.-J., J.-C. Lo, G.-H. Chen, J. Callis, H. Fu and K.-C. Yeh (2013). "IRT1 DEGRADATION FACTOR1, a RING E3 Ubiquitin Ligase, Regulates the Degradation of IRON-REGULATED TRANSPORTER1 in Arabidopsis." The Plant Cell **25**(8): 3039-3051.

Steinmann, T., N. Geldner, M. Grebe, S. Mangold, C. L. Jackson, S. Paris, L. Gälweiler, K. Palme and G. Jürgens (1999). "Coordinated polar localization of auxin efflux carrier PIN1 by GNOM ARF GEF." Science **286**(5438): 316-318.

Sztul, E., P.-W. Chen, J. E. Casanova, J. Cherfils, J. B. Dacks, D. G. Lambright, F.-J. S. Lee, P. A. Randazzo, L. C. Santy, A. Schürmann, I. Wilhelmi, M. E. Yohe and R. A. Kahn (2019). "ARF GTPases and their GEFs and GAPs: concepts and challenges." Molecular biology of the cell **30**(11): 1249-1271.

Takano, J., M. Tanaka, A. Toyoda, K. Miwa, K. Kasai, K. Fuji, H. Onouchi, S. Naito and T. Fujiwara (2010). "Polar localization and degradation of Arabidopsis boron transporters through distinct trafficking pathways." Proc Natl Acad Sci U S A **107**(11): 5220-5225.

Tanaka, H., S. Kitakura, R. De Rycke, R. De Groodt and J. Friml (2009). "Fluorescence imaging-based screen identifies ARF GEF component of early endosomal trafficking." Curr Biol **19**(5): 391-397.

Tanaka, H., T. Nodzyński, S. Kitakura, M. I. Feraru, M. Sasabe, T. Ishikawa, J. Kleine-Vehn, T. Kakimoto and J. Friml (2014). "BEX1/ARF1A1C is Required for BFA-Sensitive Recycling of PIN Auxin Transporters and Auxin-Mediated Development in Arabidopsis." Plant and Cell Physiology **55**(4): 737-749.

Tzafrir, I., J. A. McElver, C.-m. Liu Cm, L. J. Yang, J. Q. Wu, A. Martinez, D. A. Patton and D. W. Meinke (2002). "Diversity of TITAN functions in Arabidopsis seed development." Plant physiology **128**(1): 38-51.

Valencia, J. P., K. Goodman and M. S. Otegui (2016). "Endocytosis and Endosomal Trafficking in Plants." Annual Review of Plant Biology **67**(1): 309-335.

Vernoud, V., A. C. Horton, Z. Yang and E. Nielsen (2003). "Analysis of the small GTPase gene superfamily of Arabidopsis." Plant Physiol **131**(3): 1191-1208.

Vert, G., N. Grotz, F. Dédaldéchamp, F. Gaymard, M. L. Guerinot, J.-F. Briat and C. Curie (2002). "IRT1, an Arabidopsis Transporter Essential for Iron Uptake from the Soil and for Plant Growth." The Plant Cell **14**(6): 1223-1233.

von der Mark, C., R. Ivanov, M. Eutebach, V. G. Maurino, P. Bauer and T. Brumbarova (2020). "Reactive oxygen species coordinate the transcriptional responses to iron availability in Arabidopsis." Journal of Experimental Botany **72**(6): 2181-2195.

1233 **Yoshinari, A., Y. Toda and J. Takano** (2021). "GNOM-dependent endocytosis maintains polar
1234 localisation of the borate exporter BOR1 in Arabidopsis." Biology of the Cell **113**(5): 264-269.
1235

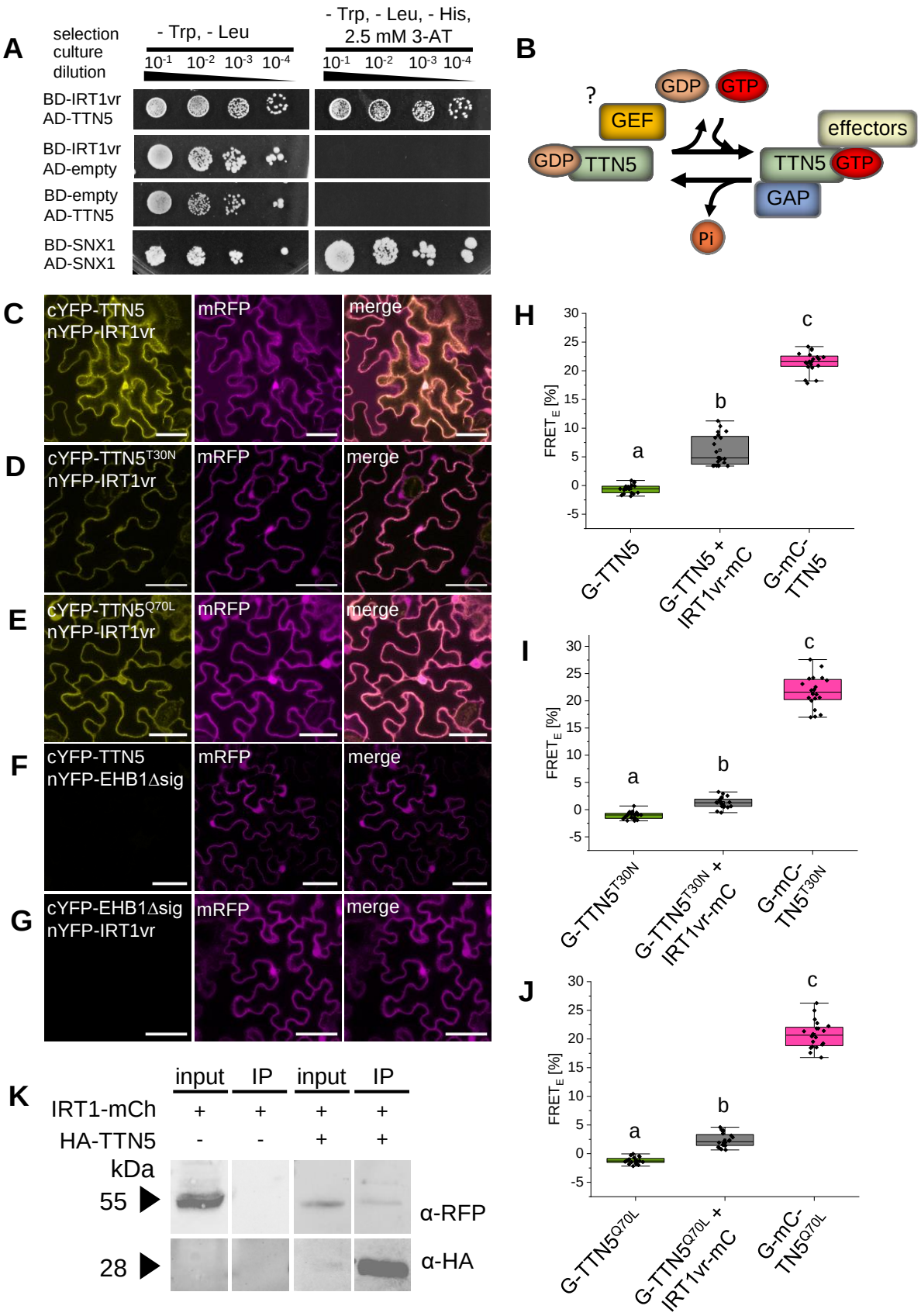
A
selection culture dilution
- Trp, - Leu
- Trp, - Leu, - His, 2.5 mM 3-AT
10-1 10-2 10-3 10-4
BD-IRT1vr AD-TTN5
BD-IRT1vr AD-empty
BD-empty AD-TTN5
BD-SNX1 AD-SNX1
B
?
GDP
GTP
GEF
effectors
GDP
TTN5
TTN5
GTP
GAP
Pi
C
cYFP-TTN5 nYFP-IRT1vr
mRFP
merge
D
cYFP-TTN5T30N nYFP-IRT1vr
E
cYFP-TTN5Q70L nYFP-IRT1vr
F
cYFP-TTN5 nYFP-EHB1Δsig
G
cYFP-EHB1Δsig nYFP-IRT1vr
H
FRETE [%]
a
b
c
G-TTN5
G-TTN5 + IRT1vr-mC
G-mC-TTN5
I
G-TTN5T30N
G-TTN5T30N + IRT1vr-mC
G-mC-TN5T30N
J
G-TTN5Q70L
G-TTN5Q70L + IRT1vr-mC
G-mC-TN5Q70L
K
input IP input IP
IRT1-mCh + + + +
HA-TTN5 - - + +
kDa
55
28
α-RFP
α-HA

Figure 1. TTN5 interacts with IRT1 via the cytosolic loop and variable region IRT1vr.

(A), Targeted Y2H assay between BD-IRT1vr (IRT1-variable region, vr) and AD-TTN5. Yeast cotransformation samples were spotted in 10-fold dilution series (A_{600} = 10^1-10^4) on double selective (LW; control) and triple selective +0.5 mM 3-AT (LWH, selection for protein interactions) SD-plates. SNX1/SNX1, positive control (Pourcher et al. 2010), BD-IRT1vr/AD-empty and BD-empty/AD-TTN5 respective negative controls. (B), Schematic representation of the switching mechanism of small GTPases based on TTN5. TTN5 can switch between an inactive GDP-loaded form to an active GTP-loaded one. Many small GTPases require a guanidine exchange factor (GEF) for nucleotide exchange (Vernoud et al. 2003). However, TTN5 has unusually high intrinsic GDP to GTP nucleotide exchange capability and help by a GEF may not be needed (indicated by space between TTN5 and GEF). Nevertheless, it is not excluded that TTN5 can interact with a GEF (indicated by a question mark) in plant cells. GTP hydrolysis has to be catalyzed by a GTPase-activating protein (GAP) (Mohr et al. 2024). GTP-loaded TTN5 can interact with effector proteins for signal transition. (C-G), Validation of TTN5-IRT1vr interaction by bimolecular fluorescence complementation (BiFC) of split YFP. Proteins of interest are fused either to the C- or N-terminal half of split-YFP in this assay. Potential interaction is indicated by a reconstituted YFP signal. mRFP serves as a transformation control. (C-E), nYFP-IRT1vr showed YFP complementation in combination with (C) cYFP-TTN5, (D) cYFP-TTN5^{T30N} and cYFP-TTN5^{Q70L} variants. The complementation takes place in nucleus and cytoplasm predominantly. (F-G), The combinations (F) cYFP-TTN5/nYFP-EHB1Δsig and (G) cYFP-EHB1Δsig/nYFP-IRT1vr served as negative controls. Each combination was tested a minimum of three times with comparable results. Scale bar 50 µm. (H-J), Confirmed interaction via Förster resonance energy transfer (FRET)-acceptor photobleaching (APB). Significant increase of FRET-efficiency ($FRET_E$) between IRT1vr-mCherry (IRT1vr-mC) and (H) GFP-TTN5 (G-TTN5), (I) GFP-TTN5^{T30N} (G-TTN5^{T30N}) or (J) GFP-TTN5^{Q70L} (G-TTN5^{Q70L}) indicate short protein distances. GFP-fusions are donor-only samples and serve as a negative control. GFP-mCherry-tagged constructs show intra-molecular FRET as a respective positive control. Each combination was tested a minimum of three times with comparable results with a minimum of ten individual measurements ($n \geq 10$). The box represents the 25–75th percentiles, and the median is indicated. The whiskers show the 5th and 95th percentiles. One-way ANOVA with Tukey post-hoc test was performed. Different letters indicate statistical significance ($p < 0.05$). (K) *In planta* coimmunoprecipitation (Co-IP) experiment demonstrating interaction between full-length IRT1-mCherry (proIRT1::IRT1Q80-mCherry) and HA_3-TTN5 (pro35S::HA_3-TTN5) using Arabidopsis roots carrying both transgenes or only IRT1-mCherry grown in parallel under Fe-deficient conditions. Following protein complex extraction, coimmunoprecipitation was conducted with anti-HA antibody. HA_3-TTN5 protein was enriched by the pull-down, resulting in an increased band intensity in the elution (IP) fraction compared to the input. IRT1Q80-mCherry protein was copurified with HA_3-TTN5 in two out of three repetitions. No coimmunoprecipitation is detected in the negative control in the absence of HA_3-TTN5 protein.

.

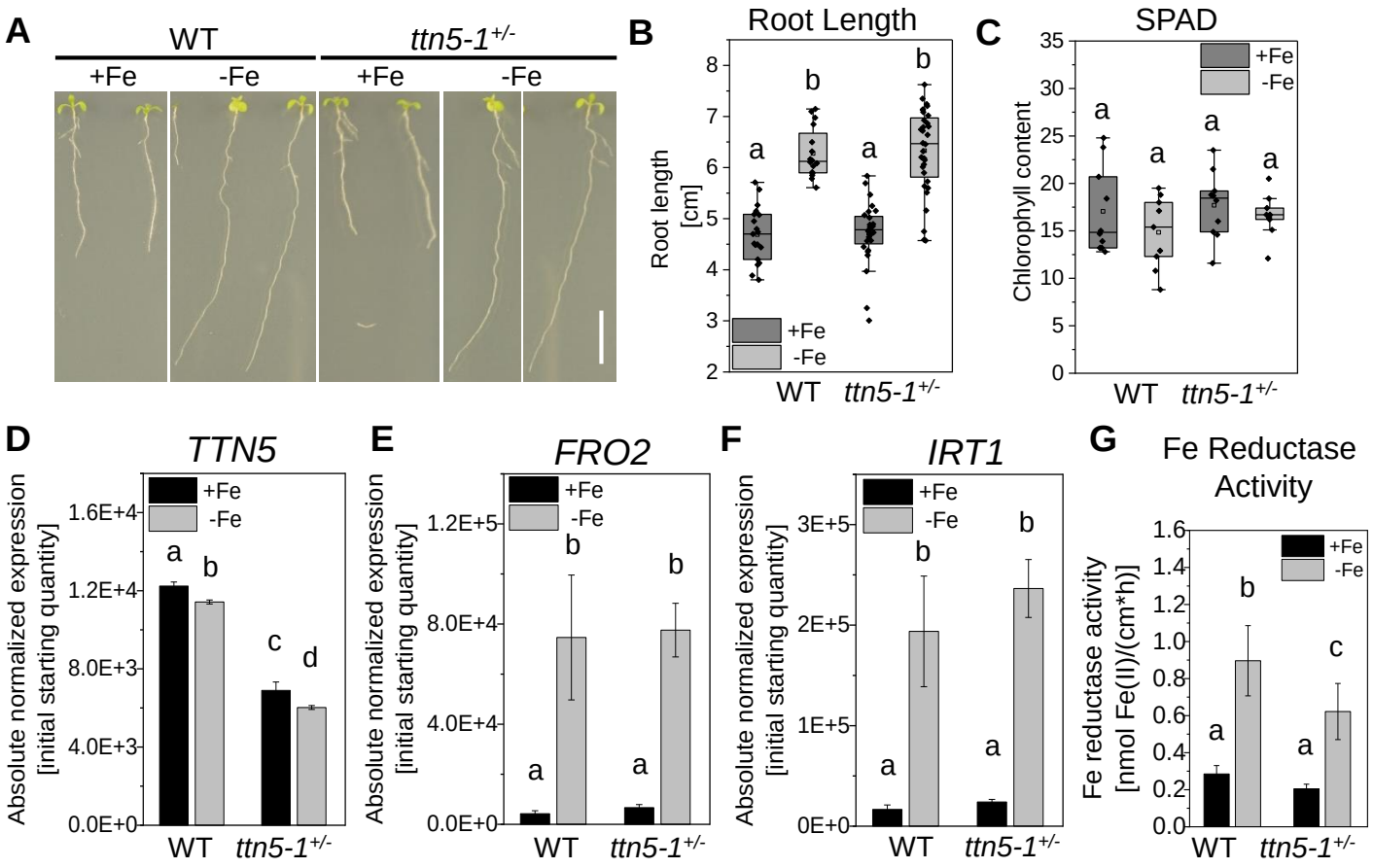
A
WT
ttn5-1+/-
+Fe
-Fe
+Fe
-Fe
B
Root Length
Root length [cm]
+Fe
-Fe
WT
ttn5-1+/-
C
SPAD
Chlorophyll content
+Fe
-Fe
WT
ttn5-1+/-
D
TTN5
Absolute normalized expression [initial starting quantity]
+Fe
-Fe
WT
ttn5-1+/-
E
FRO2
Absolute normalized expression [initial starting quantity]
+Fe
-Fe
WT
ttn5-1+/-
F
IRT1
Absolute normalized expression [initial starting quantity]
+Fe
-Fe
WT
ttn5-1+/-
G
Fe Reductase Activity
Fe reductase activity [nmol Fe(II)/(cm*h)]
+Fe
-Fe
WT
ttn5-1+/-

Figure 2. Heterozygous *ttn5-1*$^{+/-}$ seedlings can have an Fe reductase phenotype.

Heterozygous *ttn5-1*$^{+/-}$ and their wild type sibling seedlings were grown on +/-Fe Hoagland plates for ten days (A, B) or in the two-week system (C-H). All plants were individually genotyped as wild type or *ttn5-1*$^{+/-}$. Note that homozygous *ttn5-1*$^{+/+}$ are embryo-lethal. (A), + and -Fe-grown *ttn5-1*$^{+/-}$ seedlings appeared phenotypically as wild type (WT) siblings. Scale bar 1 cm. (B), Quantified root length of (A). Root length increased under Fe-deficient conditions (-Fe, light grey boxes) compared to sufficient conditions (+Fe, dark grey boxes), similar in *ttn5-1*$^{+/-}$ and wild type siblings (+Fe: WT n = 19; *ttn5-1*$^{+/-}$ n = 28; -Fe: WT n = 16; *ttn5-1*$^{+/-}$ n = 32). The box represents the 25–75th percentiles, and the median is indicated. The whiskers show the 5th and 95th percentiles. (C), Soil Plant Analysis Development (SPAD) values, reflecting chlorophyll amounts, were similar under both Fe conditions (-Fe, light grey boxes; +Fe, dark grey boxes) and comparable between the plants (+Fe: n = 10; -Fe: n = 9). The box represents the 25–75th percentiles, and the median is indicated. The whiskers show the 5th and 95th percentiles. (D-F), Gene expression data determined by RT-qPCR of *TTN5, FRO2* and *IRT1* in *ttn5-1*$^{+/-}$ roots compared to wild type siblings in Fe-sufficient (+Fe, black bars) or -deficient (-Fe, grey bars) conditions. (D), *TTN5* expression levels were higher in +Fe than -Fe conditions in wild type and *ttn5-1*$^{+/-}$ seedlings. Expression was about half in mutant versus wild type (E-F) *FRO2* and *IRT1* expression was induced upon Fe deficiency versus sufficiency in wild type and *ttn5-1*$^{+/-}$ seedlings in comparable amounts. Data was obtained from three biological replicates (n = 3). (G), Root ferric reductase activity determined by the Fe^{2+}-ferrozine assay at 562 nm. Iron reductase activity was increased upon Fe deficiency in wild type. Same was found in *ttn5-1*$^{+/-}$ sibling seedlings under Fe deficiency but to lesser extent. The assay was performed with three (wild type) and four (*ttn5-1*$^{+/-}$) biological replicates (WT n = 3; *ttn5-1*$^{+/-}$ n = 4). The experiment was repeated in total three times. In two cases, Fe reductase activity was reduced in *ttn5-1*$^{+/-}$ compared with wild type siblings (one representative experiment shown), and once it was not different. One-way ANOVA with Tukey as post-hoc test was performed. Different letters indicate statistical significance ($p < 0.05$).

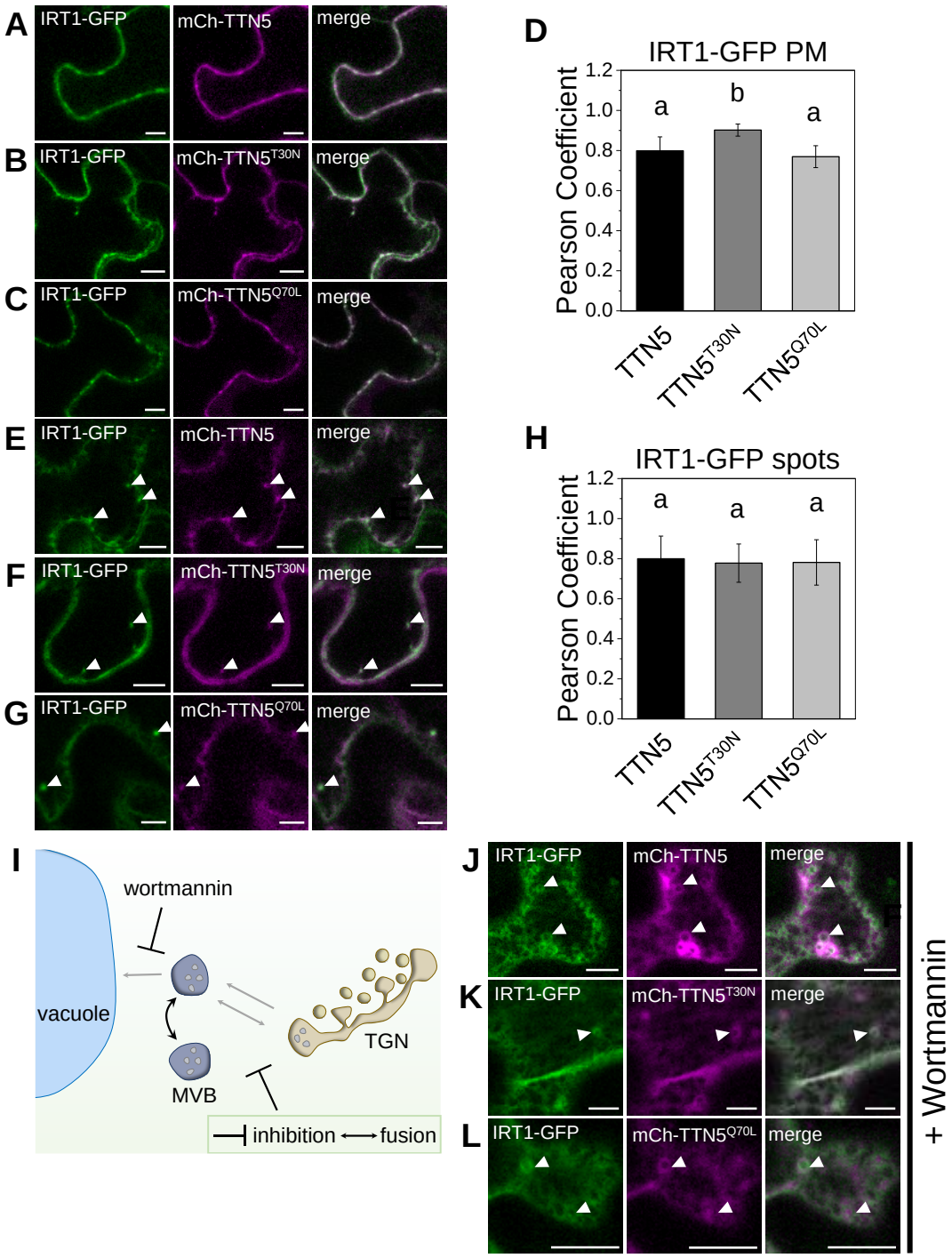
A
IRT1-GFP
mCh-TTN5
merge
B
IRT1-GFP
mCh-TTN5T30N
merge
C
IRT1-GFP
mCh-TTN5Q70L
merge
E
IRT1-GFP
mCh-TTN5
merge
F
IRT1-GFP
mCh-TTN5T30N
merge
G
IRT1-GFP
mCh-TTN5Q70L
merge
D
IRT1-GFP PM
Pearson Coefficient
1.2
1.0
0.8
0.6
0.4
0.2
0.0
a
b
a
TTN5
TTN5T30N
TTN5Q70L
H
IRT1-GFP spots
Pearson Coefficient
1.2
1.0
0.8
0.6
0.4
0.2
0.0
a
a
a
TTN5
TTN5T30N
TTN5Q70L
I
wortmannin
vacuole
MVB
TGN
inhibition
fusion
J
IRT1-GFP
mCh-TTN5
merge
K
IRT1-GFP
mCh-TTN5T30N
merge
L
IRT1-GFP
mCh-TTN5Q70L
merge
+ Wortmannin

Figure 3. TTN5 and IRT1 fluorescence protein signals colocalize at the plasma membrane and in multi-vesicular bodies (MVBs) in *N. benthamiana* leaf pavement cells.

Fluorescent signals of mCherry-TTN5 and its mutant derivatives mCherry-TTN5^{T30N} and mCherry-TTN5^{Q70L} were colocalized with IRT1-GFP (pro35S::IRT1-GFP) expression in *N. benthamiana* leaf pavement cells. (A-C), Fluorescent signals of mCherry-TTN5 and mCherry-TTN5 variants expressing constructs were present at the plasma membrane and in distinct spots together with IRT1-GFP signal. (D), JACoP-based colocalization analysis of mCherry-TTN5 and variants with IRT1-GFP (Bolte and Cordelières, 2006) performed with ImageJ (Schneider et al. 2012). Comparison of Pearson's coefficients for IRT1-GFP with mCherry-TTN5, mCherry-TTN5^{T30N} and mCherry-TTN5^{Q70L} at the plasma membrane (PM). Fluorescent signals of mCherry-TTN5^{T30N} construct were more present at the PM compared to signals of mCherry-TTN5 and mCherry-TTN5^{Q70L}. (E-G), Internalized fluorescent signals of IRT1-GFP expression were present in vesicle-like structures positively labelled by mCherry-TTN5 and mCherry-TTN5 variant signals. (H), Comparison of Pearson's coefficients for IRT1-GFP with mCherry-TTN5, mCherry-TTN5^{T30N} and mCherry-TTN5^{Q70L} in internalized spots. Fluorescent signals of all mCherry-TTN5 construct colocalized in a similar way with IRT1-GFP signals. (I), Schematic illustration of the inhibiting function of the fungal metabolite wortmannin on cellular trafficking routes between the vacuole and the *trans*-Golgi network via MVBs, leading to swelling of MVBs. (J-L), Cells were treated with wortmannin (10 µM). Swollen MVBs are visible with the GFP- and mCherry-channel, respectively. Colocalization is indicated with filled arrowheads. The experiments with JACoP analyses were repeated in a minimum of three times ($n \geq 3$). One-way ANOVA with Fisher-LSD as post-hoc test was performed. Different letters indicate statistical significance ($p < 0.05$). Scale bar 10 µm.

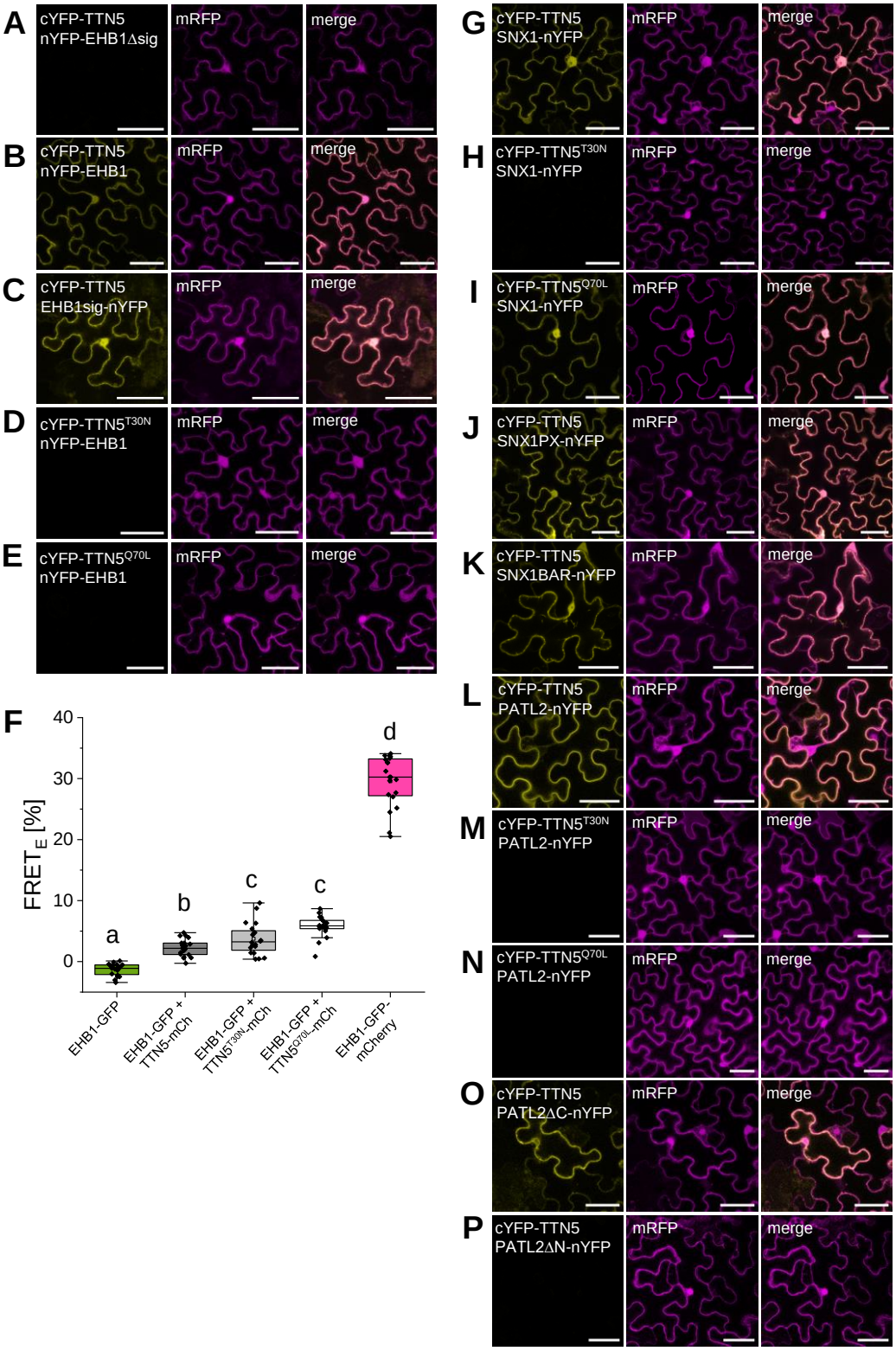
A
cYFP-TTN5
nYFP-EHB1Δsig
mRFP
merge
B
cYFP-TTN5
nYFP-EHB1
mRFP
merge
C
cYFP-TTN5
EHB1sig-nYFP
mRFP
merge
D
cYFP-TTN5T30N
nYFP-EHB1
mRFP
merge
E
cYFP-TTN5Q70L
nYFP-EHB1
mRFP
merge
F
FRETE [%]
40
30
20
10
0
a
b
c
c
d
EHB1-GFP
EHB1-GFP + TTN5-mCh
EHB1-GFP + TTN5T30N-mCh
EHB1-GFP + TTN5Q70L-mCh
EHB1-GFP-mCherry
G
cYFP-TTN5
SNX1-nYFP
mRFP
merge
H
cYFP-TTN5T30N
SNX1-nYFP
mRFP
merge
I
cYFP-TTN5Q70L
SNX1-nYFP
mRFP
merge
J
cYFP-TTN5
SNX1PX-nYFP
mRFP
merge
K
cYFP-TTN5
SNX1BAR-nYFP
mRFP
merge
L
cYFP-TTN5
PATL2-nYFP
mRFP
merge
M
cYFP-TTN5T30N
PATL2-nYFP
mRFP
merge
N
cYFP-TTN5Q70L
PATL2-nYFP
mRFP
merge
O
cYFP-TTN5
PATL2ΔC-nYFP
mRFP
merge
P
cYFP-TTN5
PATL2ΔN-nYFP
mRFP
merge

Figure 4. TTN5 interacts with IRT1 regulators EHB1, SNX1 and PATL2.

(A-E, G-P), Bimolecular fluorescence complementation (BiFC) of split YFP experiments with TTN5 and known IRT1 regulators EHB1 (Khan et al. 2019), SNX1 (Ivanov et al. 2014) and PATL2 (Hornbergs et al. 2022). mRFP expression serves as a transformation control. (A-E), TTN5 interacts with EHB1 via the sig domain. (B) TTN5 and EHB1 showed complementation whereas (D, E) variants were not able to complement split-YFP. (A, C) TTN5 was tested together with EHB1sig (signature domain, sig domain only) and with EHB1 harboring a deletion of the CAR sig domain (sig domain defined in (Rodriguez et al. 2014; Khan et al. 2019), EHB1∆sig). Deletion of the sig domain resulted in loss of complementation. (F), Interaction between EHB1-GFP (donor) with TTN5-mCherry and TTN5-mCherry variants (acceptor) was confirmed by FRET-APB. EHB1-GFP as donor-only sample (negative control), EHB1-GFP-mCherry for intra-molecular FRET (positive control). In this assay, TTN5 variants interacted with EHB1. Each combination was tested a minimum of three times with a minimum of ten individual measurements ($n \geq 10$) with comparable results. The box represents the 25–75th percentiles, and the median is indicated. The whiskers show the 5th and 95th percentiles. (G-K), BiFC showing that TTN5 interacts with SNX1. (G) TTN5 and (I) TTN5^{Q70L} showed complemented YFP signal together with SNX1. No YFP fluorescence was detectable for (H) TTN5^{T30N} with SNX1. (J, K), An interaction took place between TTN5 and the (J) PX and (K) the BAR domain of SNX1. (L-P), BiFC showing that TTN5 interacted with PATL2. (L) PATL2 showed complemented YFP signal with N-terminally-tagged TTN5. (M) TTN5^{T30N} and (N) TTN5^{Q70L} did not complement YFP with PATL2. (O-P), Deletion mutants of PATL2 showed dependency of the N-terminus for complementation with TTN5. (O) YFP signal was visible for PATL2 N-terminus (PATL2ΔC). (P) On the other hand, the C-terminus alone (PATL2ΔN) had no detectable YFP. Every construct was tested a minimum of three times ($n \geq 3$) with similar results. Scale bar 50 µm. One-way ANOVA with Tukey post-hoc test was performed. Different letters indicate statistical significance ($p < 0.05$).

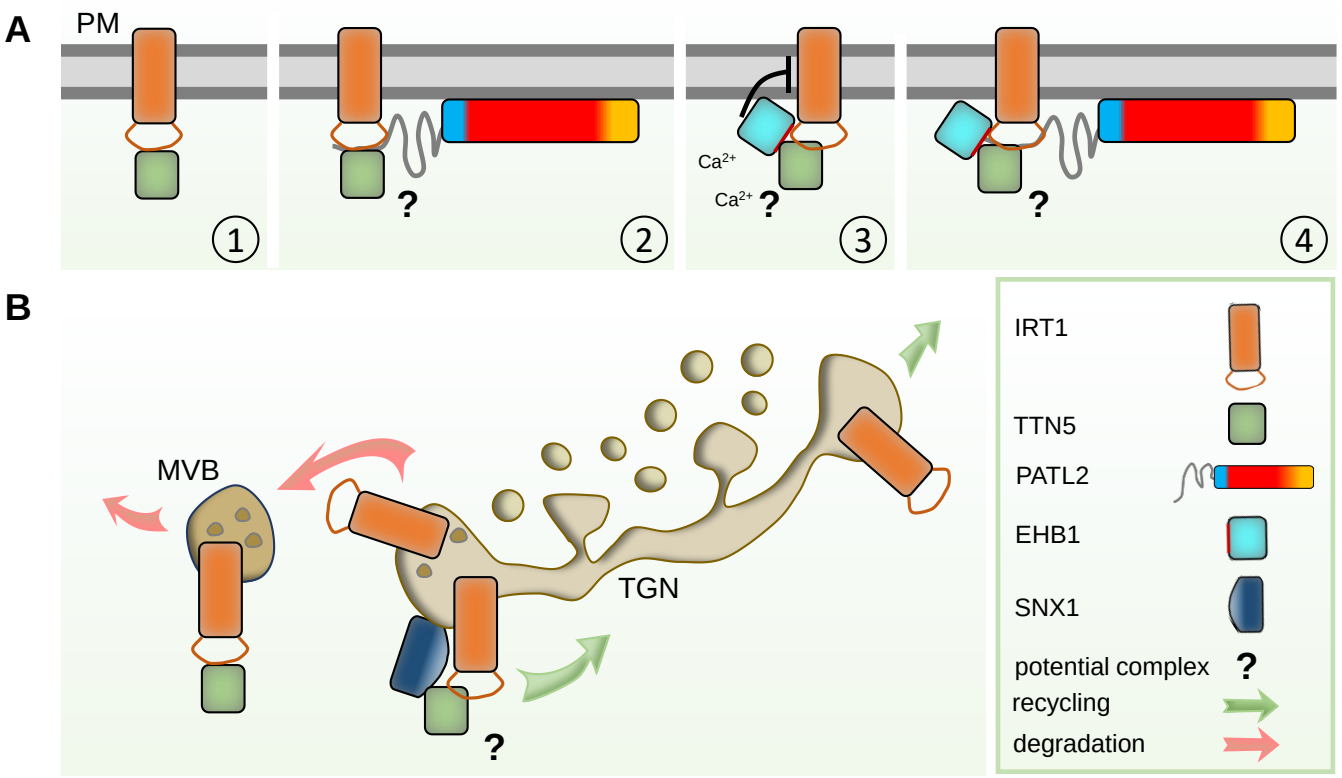
A
PM
1
?
2
Ca2+
Ca2+ ?
3
?
4
B
MVB
TGN
?
IRT1
TTN5
PATL2
EHB1
SNX1
potential complex ?
recycling
degradation

Figure 5. Summary model: Action of TTN5 within the IRT1-regulatory network.

A schematic overview of the identified TTN5 interactors within the IRT1-regulatory network (A) at the plasma membrane (PM) or (B) in the endomembrane compartments of the *trans*-Golgi network (TGN) or multivesicular body (MVB). IRT1 undergoes a constant cycling due to endocytosis from the plasma membrane and either degradation via the lytic pathway in the vacuole or recycling back to the plasma membrane. (A), We identified TTN5 interaction with the large cytosolic, variable region of IRT1. TTN5 and IRT1 colocalized at the plasma membrane (1). PATL2 interacts with the large cytosolic, variable region of IRT1 (IRT1vr) via its N-terminus and may be involved in α-tocopherol recruitment to the membrane, to prevent lipid peroxidation induced by IRT1-related iron import (Hornbergs et al. 2022). TTN5 also interacts with the N-terminus of PATL2. A potential TTN5-PATL2-IRT1 complex formation is suggested (2). EHB1 interacts with the large cytosolic, variable region of IRT1 via its signature (sig) domain and inhibits IRT1 function at the plasma membrane in a Ca^{2+}-dependent manner (Khan et al. 2019). TTN5 also interacted with EHB1 via the sig domain. A potential TTN5-EHB1-IRT1 complex formation is suggested (3). A possible quadruple complex of IRT1, TTN5, PATL2 and EHB1 (4). (B) We found that IRT1 colocalized with SNX1 (Ivanov et al. 2014) and TTN5 in the TGN. IRT1 and TTN5 also colocalized in MVBs. The protein representations are explained in the legend, a potential protein complex that may form, is indicated by a question mark.

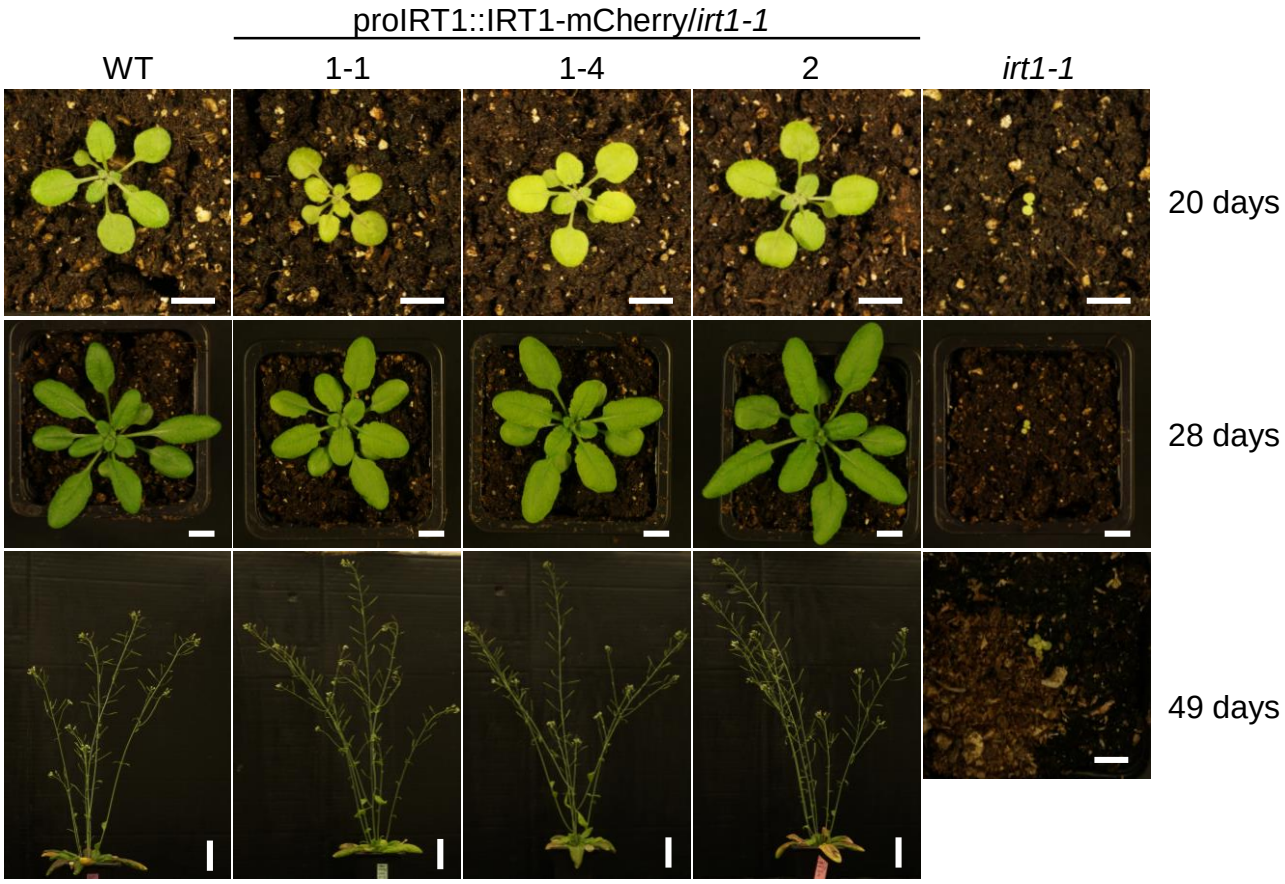
proIRT1::IRT1-mCherry/irt1-1
WT
1-1
1-4
2
irt1-1
20 days
28 days
49 days

Supplemental Figure S1. IRT1Q80-mCherry complements *irt1-1* knockout phenotypes. Complementation of the rosette growth defect, leaf chlorosis and reproductive capacity of *irt1-1* (SALK_054554) by IRT1-mCherry. Seedlings of wild type (WT), proIRT1::IRT1-mCherry/*irt1-1* (briefly IRT1-mCherry) and *irt1-1* were grown on soil. Rosettes were imaged after 20, 28 and 49 days. IRT1-mCherry lines complemented both the defect in rosette growth, leaf chlorosis, and silique formation of the *irt1-1* mutant and were comparable to the wild type. Scale bar horizontal´: 1 cm, vertical: 5 cm.

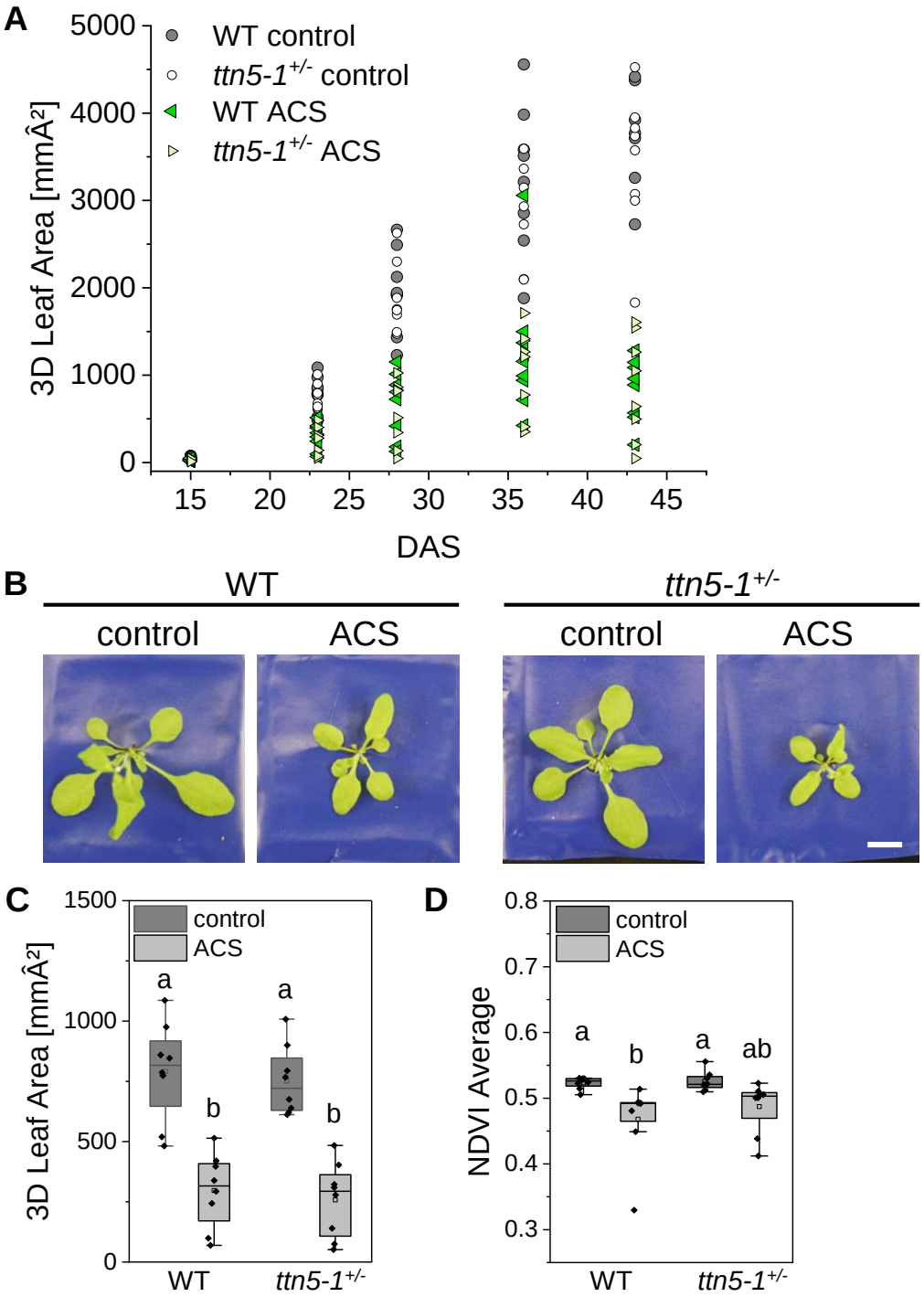
A
WT control
ttn5-1+/- control
WT ACS
ttn5-1+/- ACS
3D Leaf Area [mmÂ²]
DAS
B
WT
ttn5-1+/-
control
ACS
control
ACS
C
control
ACS
3D Leaf Area [mmÂ²]
WT
ttn5-1+/-
D
control
ACS
NDVI Average
WT
ttn5-1+/-

Supplemental Figure S2. Alkaline calcareous soil similarly impacts growth of *ttn5-1*$^{+/-}$ and wild type plants.

Heterozygous *ttn5-1*$^{+/-}$ and their wild type sibling seedlings were grown in comparison on +Fe Hoagland plates for 9 days and then transferred to alkaline, calcareous soil (ACS) or control conditions. Phenotypical analysis was conducted 15, 23, 28, 35 and 43 days after sowing using PlantEye (Phenospex). (A), Growth of wild type (WT; dark colors) and *ttn5-1*$^{+/-}$ (bright colors) plants on both, control (circle) and ACS (triangle) soil conditions determined by 3D leaf area. The parameter "3D Leaf Area" represents the area of the surface of the whole scanned object visible from straight above, including rosettes, stems and inflorescences. ACS condition led to a reduced 3D leaf area for both wild type and *ttn5-1*$^{+/-}$. (B-D), Detailed phenotypical analysis of WT and *ttn5-1*$^{+/-}$ after 23 days. (B) Images of WT and *ttn5-1*$^{+/-}$ on both soil conditions. ACS condition led to a reduced rosette size for both. Scale bar 1 cm. (C), PlantEye analysis confirmed a significant reduced 3D leaf area on ACS compared to control conditions for both wild type (WT) and *ttn5-1*$^{+/-}$ plants in a similar amount. The box represents the 25–75th percentiles, and the median is indicated. The whiskers show the 5th and 95th percentiles**.** (D), Normalized difference vegetation index (NDVI) was used as a correlation factor for photosynthetic efficiency. For the NDVI, the reflectance of red (RED, 624-634 nm) and near-infrared (NIR, 720-750 nm) light is determined at all points of the scanned object, that are reached by the light. The NDVI is then calculated as (NIR – RED) / (NIR + RED) for each point and the average over the object is determined. WT plants grown in ACS condition had a significant reduced NDVI compared to control soil while this effect was less the case for *ttn5-1*$^{+/-}$ plants. The experiment was performed with eight biological replicates (n = 8). The box represents the 25–75th percentiles, and the median is indicated. The whiskers show the 5th and 95th percentiles**.** One-way ANOVA with Tukey post-hoc test was performed. Different letters indicate statistical significance ($p < 0.05$).

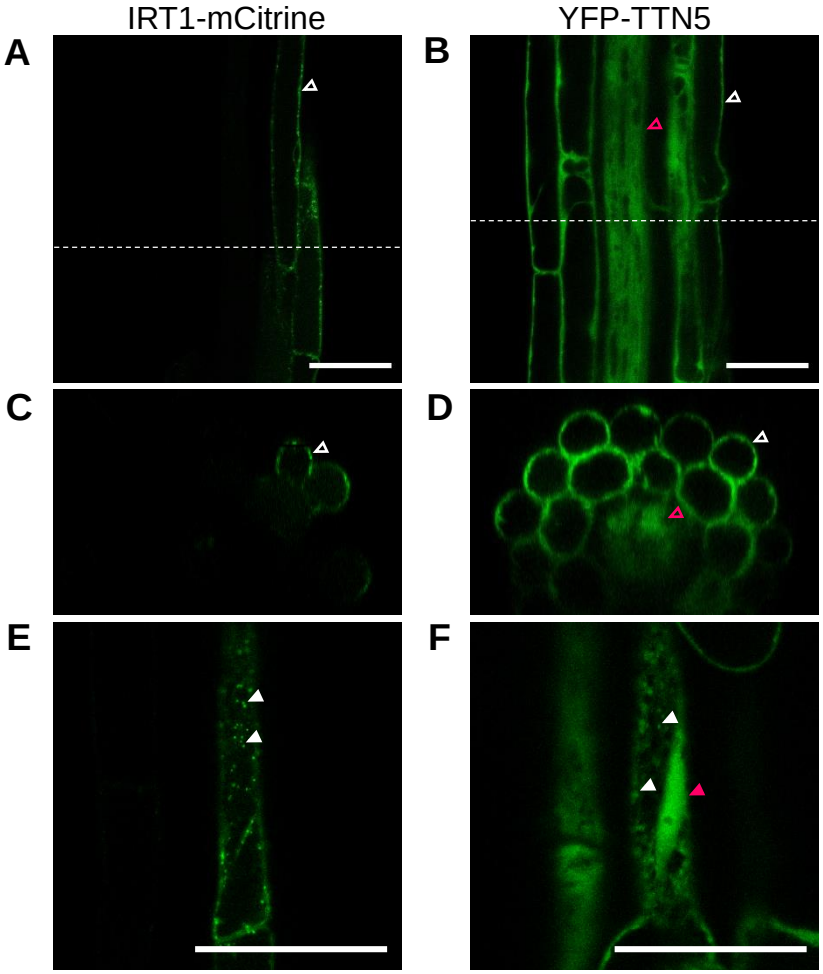
IRT1-mCitrine
YFP-TTN5
A
B
C
D
E
F

Supplemental Figure S3. Localization of IRT1 and TTN5 fluorescence fusion proteins in the Arabidopsis root elongation zone.

(A, C, E) IRT1-mCitrine localization in proIRT1::IRT1-mCitrine/*irt1-1* seedling roots (line previously described in Dubeaux et al. 2018; Hornbergs et al. 2023) in comparison with (B, D, F) YFP-TTN5 localization in pro35S::YFP-TTN5/WT seedling roots (line previously described in Mohr et al. 2024) in the root elongation zone. Plants were grown on plates side by side. (A, B), Longitudinal confocal sections through the stele. (A) IRT1-mCitrine was present at the plasma membrane of epidermal cells (empty white arrowhead). (B) Fluorescent signal of YFP-TTN5 roots was localized at the plasma membrane of epidermal cells and other cell types, as well as in the stele (empty magenta arrowhead). Dotted white lines indicate the position of the cross sections shown in C and D. (C-D), Cross confocal sections highlighting (C) IRT1-mCitrine in epidermal cells compared to (D) nearly ubiquitously localized fluorescent signal in YFP-TTN5 roots. (E-F), Longitudinal section through the epidermis regions. Next to plasma membrane, (E) IRT1-mCitrine and (F) YFP-TTN5 were present in intracellular spots (filled white arrowheads). YFP-TTN5 was also detected in the nucleus (filled magenta arrowhead). The experiment was repeated in a minimum of three times ($n \geq 3$). Scale bar 10 µm.

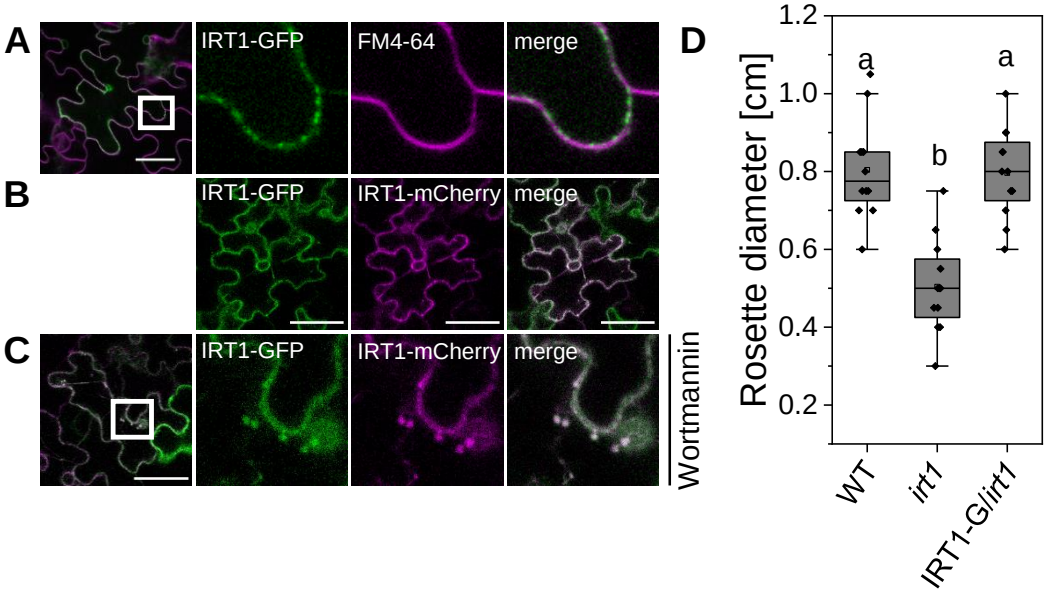

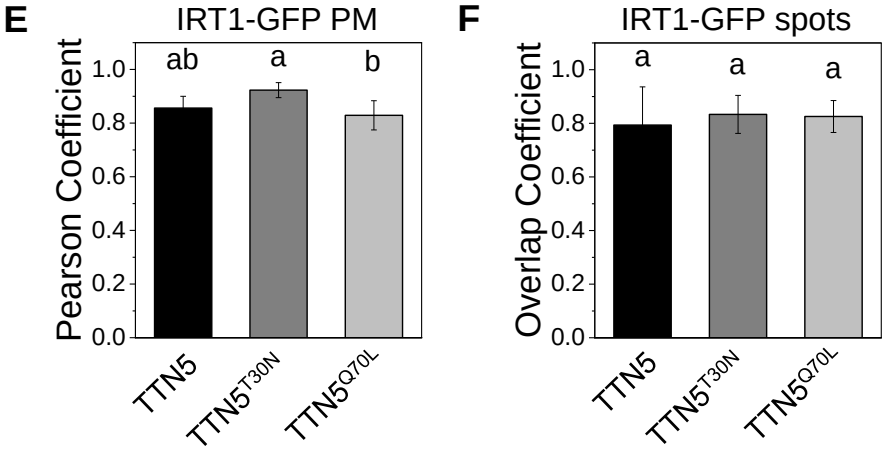

G

Channel		Colocalization spots	
GFP/YFP	mRFP/mCh	GFP/mRFP	mRFP/GFP
IRT1-GFP	mCh-TTN5	64.10±25.58	41.13±28.78
IRT1-GFP	mCh-TTN5^{T30N}	54.44±30.81	36.65±8.25
IRT1-GFP	mCh-TTN5^{Q70L}	82.59±12.71	36.34±9.66

Supplemental Figure S4. IRT1 colocalization analysis at the plasma membrane and in intracellular spots.

(A), Plasma membrane dye FM4-64 indicated IRT1-GFP localization at the plasma membrane. IRT1-GFP is present in a spotted structure, indicating regions of higher transporter accumulation. (B-C), IRT1-GFP colocalized with IRT1-mCherry (Ivanov et al., 2014) (B) at the plasma membrane (PM) and (C) in swollen intracellular spots after wortmannin treatment (10 µM), confirming correct localization of IRT1-GFP. The experiments were repeated in a minimum of three times (n ≥ 3). Scale bar 50 µm. (D), Complementation of rosette growth defect of *irt1-1* by IRT1-GFP. Rosette sizes of *irt1-1* and pro35S::IRT1-GFP/*irt1-1* were measured 14 days after sowing. IRT1-GFP complemented the growth defect of *irt1-1*. The experiment was conducted once with twelve biological replicates (n = 12). The box represents the 25–75th percentiles, and the median is indicated. The whiskers show the 5th and 95th percentiles. (E-G), JACoP-based colocalization analysis of mCherry-TTN5 and variants with IRT1-GFP (Bolte and Cordelières, 2006) performed with ImageJ (Schneider et al., 2012). See also Figure 3A-H. (E-F), Comparison of (from left to right) Overlap coefficients for IRT1-GFP with mCherry-TTN5, mCherry-TTN5^{T30N} and mCherry-TTN5^{Q70L} (E) at the plasma membrane and (F) in vesicle-like structures. (G), Object-based analysis was performed for spotted-structures based on distance between geometrical centers of signals. Analyses were conducted in three replicates each (n = 3). One-way ANOVA with Fisher-LSD post-hoc test was performed. Different letters indicate statistical significance ($p < 0.05$).

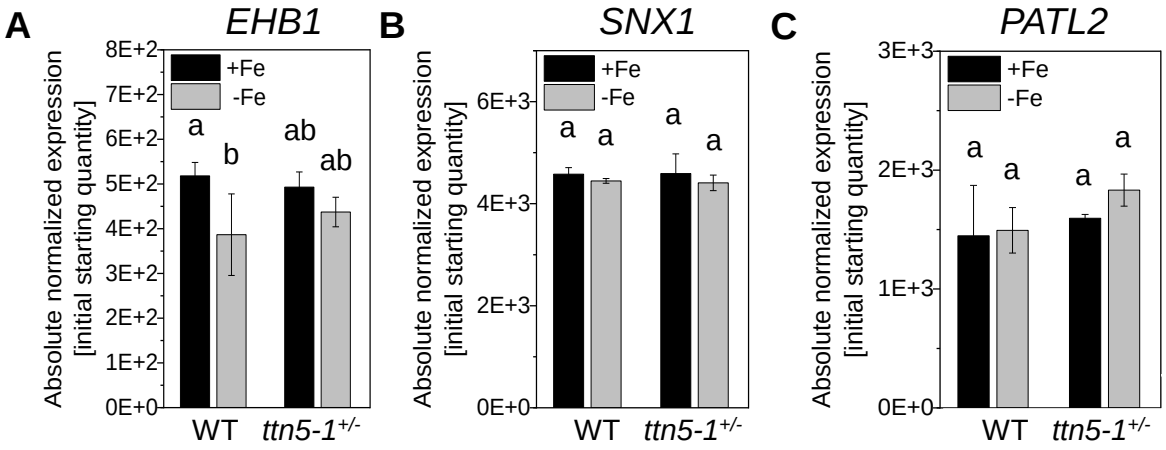
A
EHB1
Absolute normalized expression
[initial starting quantity]
8E+2
7E+2
6E+2
5E+2
4E+2
3E+2
2E+2
1E+2
0E+0
+Fe
-Fe
a
b
ab
ab
WT
ttn5-1+/-
B
SNX1
Absolute normalized expression
[initial starting quantity]
6E+3
4E+3
2E+3
0E+0
+Fe
-Fe
a
a
a
a
WT
ttn5-1+/-
C
PATL2
Absolute normalized expression
[initial starting quantity]
3E+3
2E+3
1E+3
0E+0
+Fe
-Fe
a
a
a
a
WT
ttn5-1+/-

Supplemental Figure S5. Gene expression of *EHB1*, *SNX1* and *PATL2* is not affected in *ttn5-1*$^{+/-}$ plants.

Gene expression data by RT-qPCR of *EHB1*, *SNX1* and *PATL2* in *ttn5-1*$^{+/-}$ roots compared to wild type sibling roots. Plants were grown in the two-week system in Fe-sufficient (+Fe, black bars) or -deficient (-Fe, grey bars) conditions. See also Figure 2D-F. (A), *EHB1* expression was down-regulated under Fe-deficient conditions in wild type seedlings, while expression levels were not differing in *ttn5-1*$^{+/-}$ seedlings under both Fe supply conditions. (B), *SNX1* expression was not altered between Fe-sufficient or -deficient conditions in wild type and *ttn5-1*$^{+/-}$seedlings. (C), *PATL2* expression did not change upon Fe supply in both wild type and *ttn5-1*$^{+/-}$seedlings. Data were obtained from three biological replicates (n = 3). One-way ANOVA with Fisher-LSD post-hoc test was performed. Different letters indicate statistical significance ($p < 0.05$).